IFT-UAM/CSIC-07-38

A Gravitational Wave Background from Reheating after Hybrid Inflation

Juan García-Bellido, Daniel G. Figueroa and Alfonso Sastre
Departamento de Física Teórica, Universidad Autónoma de Madrid, Cantoblanco, 28049 Madrid, Spain
Instituto de Física Teórica CSIC-UAM, Universidad Autónoma de Madrid, Cantoblanco, 28049 Madrid, Spain
(Dated: November 26th, 2007)

The reheating of the universe after hybrid inflation proceeds through the nucleation and subsequent collision of large concentrations of energy density in the form of bubble-like structures moving at relativistic speeds. This generates a significant fraction of energy in the form of a stochastic background of gravitational waves, whose time evolution is determined by the successive stages of reheating: First, tachyonic preheating makes the amplitude of gravity waves grow exponentially fast. Second, bubble collisions add a new burst of gravitational radiation. Third, turbulent motions finally sets the end of gravitational waves production. From then on, these waves propagate unimpeded to us. We find that the fraction of energy density today in these primordial gravitational waves could be significant for GUT-scale models of inflation, although well beyond the frequency range sensitivity of gravitational wave observatories like LIGO, LISA or BBO. However, low-scale models could still produce a detectable signal at frequencies accessible to BBO or DECIGO. For comparison, we have also computed the analogous gravitational wave background from some chaotic inflation models and obtained results similar to those found by other groups. The discovery of such a background would open a new observational window into the very early universe, where the details of the process of reheating, i.e. the Big Bang, could be explored. Moreover, it could also serve in the future as a new experimental tool for testing the Inflationary Paradigm.

I. INTRODUCTION

Gravitational waves (GW) are ripples in space-time that travel at the speed of light, and whose emission by relativistic bodies represents a robust prediction of General Relativity. The change in the orbital period of a binary pulsar known as PSR 1913+16 was used by Hulse and Taylor [1] to obtain indirect evidence of their existence. Although gravitational radiation has not been directly detected yet, it is expected that the present universe should be permeated by a diffuse background of GW of either an astrophysical or cosmological origin [2]. Astrophysical sources, like the gravitational collapse of supernovae or the neutron star and black hole binaries' coalescence, produce a stochastic gravitational wave background (GWB) which can be understood as coming from unresolved point sources. On the other hand, among the backgrounds of cosmological origin, we find the approximately scale-invariant background produced during inflation [3], or the GWB generated at hypothetical early universe thermal phase transitions, from relativistic motions of turbulent plasmas or from the decay of cosmic strings [2]. Fortunately, these backgrounds have very different spectral shapes and amplitudes that might, in the future, allow gravitational wave observatories like the Laser Interferometer Gravitational Wave Observatory (LIGO) [4], the Laser Interferometer Space Antenna (LISA) [5], the Big Bang Observer (BBO) [6] or the Decihertz Interferometer Gravitational Wave Observatory (DECIGO) [7], to disentangle their origin [2]. Unfortunately, due to the weakness of gravity, this task will be extremely difficult, requiring a very high accuracy in order to distinguish one background from another. It is thus important to characterize as many different sources of GW as possible.

There are, indeed, a series of constraints on some of these backgrounds, the most stringent one coming from the large-scale polarization anisotropies in the Cosmic Microwave Background (CMB), which may soon be measured by Planck [8], if the scale of inflation is sufficiently high. There are also constraints coming from Big Bang nucleosynthesis [9], since such a background would contribute as a relativistic species to the expansion of the universe and thus increase the light element abundance. There is also a constraint coming from millisecond pulsar timing [10]. Furthermore, it has recently been proposed a new constraint on a GWB coming from CMB anisotropies [11]. Most of these constraints come at very low frequencies, typically from 10^{-18} Hz to 10^{-8} Hz, while present GW detectors work at frequencies of order 1-100 Hz, and planned observatories will range from 10^{-3} Hz of LISA to 10^{3} Hz of Advanced-LIGO [2, 4]. If early universe phenomena like first order phase transitions [12, 13] or cosmic turbulence [14] occurred around the electro-weak (EW) scale, there is a chance than the GW detectors will measure the corresponding associated backgrounds. However, if such early universe processes occurred at the GUT scale, their corresponding backgrounds will go undetected by the actual detectors, since these cannot reach the required sensitivity in the high frequency range of $10^{7} - 10^{9}$ Hz, corresponding to the size of the causal horizon at that time. There are however recent proposals to cover this range [15], which may become competitive in the near future.

Moreover, present observations of the CMB anisotropies and the Large Scale Structure (LSS) distribution of matter seem to suggest that something like Inflation must have occurred in the very early universe. We ignore what drove inflation and at what scale it took place. However, approximately scale-invariant

density perturbations, sourced by quantum fluctuations during inflation, seem to be the most satisfying explanation for the CMB anisotropies. Together with such scalar perturbations one also expects tensor perturbations (GW) to be produced, with an almost scale-free power spectra [3]. Because of the weakness of gravity, this primordial inflationary GWB should decouple from the rest of matter as soon as it is produced, and move freely through the Universe till today. At present, the biggest efforts employed in the search for these primordial GW come from the indirect effect that this background has on the B-mode polarization anisotropies of the CMB [8], rather than via direct detection. The detection of such a background is crucial for early universe cosmology because it would help to determine the absolute energy scale of inflation, a quantity that for the moment is still uncertain, and would open the exploration of physics at very high energies.

In the early universe, after inflation, other backgrounds of GW could have been produced at shorter wavelengths, in a more 'classical' manner, rather than sourced by quantum fluctuations. In particular, whenever there are large and fast moving inhomogeneities in the matter distribution, one expects the emission of GW. This is much like the situation in classical electrodynamics, but with some differences. At large distances from the source, the amplitude of the electromagnetic field A_i is expressed as the first derivative of the dipole moment d_i of the charge distribution of the source, $A_i \simeq \dot{d}_i/cr$, while the amplitude of the GW is given by the second derivative of the quadrupole moment of the mass distribution, $h_{ij} \simeq G\ddot{Q}_{ij}/c^4 r$. In both cases, the larger the velocity of the matter/charge distribution, the larger the amplitude of the radiation produced. Nevertheless, the main difference between the two cases is the weakness of the strength of gravity to that of electromagnetism. Thus, in order to produce a significant amount of gravitational radiation, it is required that the motion of huge masses occurs at speeds close to that of light for the case of astrophysical sources, or a very fast motion and high density contrasts in the continuous matter distribution for the case of cosmological sources. In fact, this is believed to be the situation at the end of inflaton, during the conversion of the huge energy density driving inflation into radiation and matter at the so-called *reheating* of the Universe [16]. Such an event corresponds to the actual Big Bang of the Standard Cosmological Model.

Note that any background of GW coming from the early universe, if generated below Planck scale, immediately decoupled upon production, as can be easily understood by the following dimensional analysis argument. Assuming that gravitons were in thermal equilibrium with the early universe plasma, at a temperature T, the gravitons' cross section should be of order $\sigma \sim G^2T^2$. Then, given the graviton number density $n \sim T^3$ and velocity $v = 1$, the gravitons' interaction rate should be $\Gamma = \langle n\sigma v\rangle \sim T^5/M_p^4$. Since the Hubble rate is $H \sim T^2/M_p$, then $\Gamma \sim H\,(T/M_p)^3$, so gravitons could *not* be kept in equilibrium with the surrounding plasma for $T < M_p$. Therefore, GW produced well after Planck scale will always be decoupled from the plasma, and whatever their spectral signatures, they will retain their shape throughout the expansion of the Universe. Thus, the characteristic frequency and shape of the GWB generated at a given time should contain information about the very early state of the Universe in which they were produced. Actually, it is conceivable that, in the not so far future, the detection of these GW backgrounds could be the only way we may have to infer the physical conditions of the Universe at such high energy scales, which certainly no particle collider will ever reach. However, the same reason that makes GW ideal probes of the early universe − the weakness of gravity −, is responsible for the extreme difficulties we have for their detection on Earth. For an extensive discussion see Ref. [17].

In a recent letter [18] we described the stochastic background predicted to arise from reheating after hybrid inflation. In this paper we study in detail the various processes involved in the production of such a background, whose detection could open a new window into the very early universe. In the future, this background could also serve as a new tool to discriminate among different inflationary models, as each of these would give rise to a different GWB with very characteristic spectral features. The first stage of the energy conversion at the end of inflation, preheating [16], is known to be explosive and extremely violent, and quite often generates in less than a Hubble time the huge entropy measured today. The details of the dynamics of preheating depend very much on the model and are often very complicated because of the non-linear, non-perturbative and out-of-equilibrium character of the process itself. However, all the cases have in common that only specific resonance bands of the fields suffer an exponential instability, which makes their occupation numbers grow by many orders of magnitude. The shape and size of the spectral bands depend very much on the inflationary model. If one translates this picture into position-space, the highly populated modes correspond to large time-dependent inhomogeneities in the matter distributions which acts, in fact, as the source of GW we are looking for.

For example, in single field chaotic inflation models, the coherent oscillations of the inflaton during preheating generates, via parametric resonance, a population of highly occupied modes that behave like waves of matter. They collide among themselves and their scattering leads to homogenization and local thermal equilibrium. These collisions occur in a highly relativistic and very asymmetric way, being responsible for the generation of a stochastic GWB [21, 22, 23] with a typical frequency today of the order of $10^7 - 10^9$ Hz, corresponding to the present size of the causal horizon at the end of high-scale inflation. There is at present a couple of experiments searching for such a background, see Refs. [15], based of laser interferometry, as well as by resonant superconducting microwave cavities [26].

However, there are models like hybrid inflation in which the end of inflation is sudden [27] and the conversion into radiation occurs almost instantaneously. Indeed, since the work of Ref. [28] we know that hybrid models preheat in an even more violent way than chaotic inflation models, via the spinodal instability of the symmetry breaking field that triggers the end of inflation, irrespective of the couplings that this field may have to the rest of matter. Such a process is known as *tachyonic preheating* [28, 29] and could be responsible for copious production of dark matter particles [30], lepto and baryogenesis [31], topological defects [28], primordial magnetic fields [32], etc.

It was speculated in Ref. [22] that in (low-scale) models of hybrid inflation it might be possible to generate a stochastic GWB in the frequency range accessible to present detectors, if the scale of inflation was as low as $H_{\rm inf} \sim 1$ TeV. However, the amplitude was estimated using the parametric resonance formalism of chaotic preheating, which may not be applicable in this case. In Ref. [29] (from now on referred to as paper I), it was shown that the process of symmetry breaking proceeds via the nucleation of dense bubble-like structures moving at the speed of light, which collide and break up into smaller structures (see Figs. 7 and 8 of paper I). We conjectured at that time that such collisions would be a very strong source of GW, analogous to the GW production associated with strongly first order phase transitions [12]. As we will show in this paper, this is indeed the case during the nucleation, collision and subsequent rescattering of the initial bubble-like structures produced after hybrid inflation. During the different stages of reheating in this model, gravity waves are generated and amplified until the Universe finally thermalizes and enters into the initial radiation era of the Standard Model of Cosmology. From that moment until now, during the whole thermal history of the expansion of the universe, this cosmic GWB will be redshifted as a radiation-like fluid, totally decoupled from any other energy-matter content of the universe, such that today's ratio of energy stored in these GW to that in radiation, could range from $\Omega_{\rm GW} h^2 \sim 10^{-8}$, peacked around $f \sim 10^7$ Hz for the high-scale models, to $\Omega_{\rm GW} h^2 \sim 10^{-11}$, peacked around $f \sim 1$ Hz for the low-scale models.

Finally, let us mention that since the first paper by Khlebnikov and Tkachev [21], studing the GWB produced at reheating after chaotic inflation, it seems appropriate to reanalyze this topic in a more detailed way. The idea was extended to hybrid inflation in [22], but within the parametric resonance formalism. It was also revisited very recently in Ref. [23, 24] for the $\lambda\phi^4$ and $m^2\phi^2$ chaotic scenarios, and reanalysed again for hybrid inflation in Ref. [18], this time using the new formalism of tachyonic preheating [28, 29]. Because of the increase in computer power of the last few years, we are now able to perform precise simulations of the reheating process in a reasonable time scale. Moreover, understanding of reheating has improved, while gravitational waves detectors are beginning to attain the aimed sensitivity [4]. Furthermore, since these cosmic GWBs could serve as a deep probe into the very early universe, we should characterize in the most detailed way the information that we will be able to extract from them.

The paper is divided as follows. In Section II we briefly review the hybrid model of inflation. Section III is dedicated to our approach for extracting the power spectrum of GW from reheating. In section IV, we give a detailed account of the lattice simulations performed with two codes: our own FORTRAN parallelized computer code (running in the MareNostrum supercomputer [33] and in our UAM-IFT cluster [34]), as well as with a modified version of the publicly available C++ package LATTICEEASY [35]. Section V is dedicated to study the spatial distribution of the production of gravitational waves. In Section VI, we reproduce as a crosscheck, some of the results of [21, 23, 25] concerning the GWB produced at reheating after chaotic inflation models. Finally, in section VII, we give our conclusions and perspectives for the future.

II. THE HYBRID MODEL

Hybrid inflation models [27] arise in theories of particle physics with symmetry breaking fields ('Higgses') coupled to flat directions, and are present in many extensions of the Standard Model, both in string theory and in supersymmetric theories [19]. The potential in these models is given by

$$V(\Phi,\chi) = \lambda\left(\Phi^\dagger\Phi - \frac{v^2}{2}\right)^2 + g^2\chi^2\Phi^\dagger\Phi + \frac{1}{2}\mu^2\chi^2\,, \quad (1)$$

where the contraction $\Phi^\dagger\Phi$ should be understood as the trace $\mathrm{Tr}\,\Phi^\dagger\Phi = \frac{1}{2}|\phi|^2$. Inflation occurs along the lifted flat direction, satisfying the slow-roll conditions thanks to a large vacuum energy $\rho_0 = \lambda v^4/4$. Inflation ends when the inflaton χ falls below a critical value and the symmetry breaking field ϕ acquires a negative mass squared, which triggers the breaking of the symmetry and ends in the true vacuum, $|\phi| = v$, within a Hubble time. These models do not require small couplings in order to generate the observed CMB anisotropies; e.g. a working model with GUT scale symmetry breaking, $v = 10^{-3}\,M_P$, with a Higgs self-coupling λ and a Higgs-inflaton coupling g given by $g = \sqrt{2\lambda} = 0.05$, satisfies all CMB constraints [20], and predicts a tiny tensor contribution to the CMB polarization. The main advantage of hybrid models is that, while most chaotic inflation models can only occur at high scales, with Planck scale values for the inflaton, and $V_{\rm inf}^{1/4} \sim 10^{16}$ GeV, one can choose the scale of inflation in hybrid models to range from GUT scales all the way down to GeV scales, while the Higgs *v.e.v.* can range from Planck scale, $v = M_P$, to the Electroweak scale, $v = 246$ GeV, see Ref. [27, 31].

There are a series of constraints that a hybrid inflation model should satisfy in order to be in agreement

with observations. First of all, inflation should end in less than one e-fold, otherwise unacceptable black holes would form [36]. This can be written as the *waterfall condition* [27], $\lambda m M_P^2 \gg M^3$, which becomes

$$\frac{m}{M} \gg \frac{v^2}{M_P^2}\,. \tag{2}$$

Then there is the condition, known as the COBE normalization, that the scalar amplitude should satisfy $A_S = H^2/2\pi\dot{\phi} \simeq 5\times 10^{-5}$, which gets translated into

$$g = (n-1)\frac{M_P}{v}\sqrt{\frac{3\pi}{8}}\times 10^{-4}\, e^{(n-1)N/2} \tag{3}$$

as well as the spectral tilt,

$$n - 1 = \frac{1}{\pi}\frac{m^2}{M^2}\frac{M_P^2}{v^2} < 0.05 \tag{4}$$

and finally the fact that we have not seen so far any tensor (gravitational wave) contribution in the CMB anisotropies, $r = A_T^2/A_S^2 < 0.3$, imposes the constraint

$$\lambda^{1/4} < 2\times 10^{-3}\,\frac{M_P}{v}\,. \tag{5}$$

Taking all these conditions together, we find that a model with $v = 0.1 M_P$ is probably ruled out, while one with $v = 0.01\, M_P$ is perfectly consistent with all observations, and with reasonable values of the coupling constants, e.g. $g = 4\times 10^{-4}$ and $\lambda = 10^{-3}$. However, the lower is the scale of inflation, the more difficult it is to accommodate the amplitude of the CMB anisotropies with reasonable values of the parameters. For a scale of inflation as low as 10^{11} GeV, one must significantly finetune the couplings, although there are low scale models based on supersymmetric extensions of the standard model which can provide a good match to observations [37].

In the following sections we will show how efficient is the production of GW at reheating after hybrid inflation, using both analytical estimates and numerical simulations to derive the amplitude of the present day GWB. Reheating in hybrid inflation [27] goes through four well defined regimes: first, the exponential growth of long wave modes of the Higgs field via spinodal instability, which drives the explosive growth of all particles coupled to it, from scalars [28] to gauge fields [31] and fermions [30]; second, the nucleation and collision of high density contrast and highly relativistic bubble-like structures associated with the peaks of a Gaussian random field like the Higgs, see paper I; third, the turbulent regime that ensues after all these 'bubbles' have collided and the energy density in all fields cascades towards high momentum modes; finally, thermalization of all modes when local thermal and chemical equilibrium induces equipartition. The first three stages can be studied in detailed lattice simulations thanks to the semi-classical character of the process of preheating [38], while the last stage is intrinsically quantum and has never been studied in the lattice.

III. GRAVITATIONAL WAVE PRODUCTION

Our main purpose in this paper is to study the details of the stochastic GWB produced during the reheating of the universe after hybrid inflation (sections III, IV and V). However, we also study, albeit very briefly, the analogous background from reheating in some simple chaotic models (section VI). Thus, in this section we derive a general formalism for extracting the GW power spectrum in any scenario of reheating within the (flat) Friedman-Robertson-Walker (FRW) universe. The formalism will be simplified when applied to scenarios in which we can neglect the expansion of the universe, like in the case of most Hybrid models.

A theory with an inflaton scalar field χ interacting with other Bose fields ϕ_a, can be described by

$$\mathcal{L} = \frac{1}{2}\partial_\mu\chi\partial^\mu\chi + \frac{1}{2}\partial_\mu\phi_a\partial^\mu\phi_a + \frac{R}{16\pi G} - V(\phi,\chi) \tag{6}$$

with R the Ricci scalar. For hybrid models, we consider a generic symmetry breaking 'Higgs' field with N_c real components. Thus, we can take $\Phi^\dagger\Phi = \frac{1}{2}\sum_a \phi_a^2 \equiv |\phi|^2/2$ in (1), with a running for the number of Higgs' components, *e.g.* $N_c = 1$ for a real scalar Higgs, $N_c = 2$ for a complex scalar Higgs or $N_c = 4$ for a $SU(2)$ Higgs, etc. The effective potential (1) then becomes

$$V(\phi,\chi) = \frac{\lambda}{4}\left(|\phi|^2 - v^2\right)^2 + g^2\chi^2|\phi|^2 + \frac{1}{2}\mu^2\chi^2\,. \tag{7}$$

For chaotic scenarios, we consider a massless scalar field interacting with the inflaton via

$$V(\chi,\phi) = \frac{1}{2}g^2\chi^2\phi^2 + V(\chi)\,, \tag{8}$$

with $V(\chi)$ the inflaton's potential. Concerning the simulations we show in this paper, we concentrate in the $N_c = 4$ case for the hybrid model and consider a potential $V(\chi) = \frac{\lambda}{4}\chi^4$ for the chaotic scenario.

The classical equations of motion of the inflaton and the other Bose fields are

$$\ddot{\chi} + 3H\dot{\chi} - \frac{1}{a^2}\nabla^2\chi + \frac{\partial V}{\partial\chi} = 0 \tag{9}$$

$$\ddot{\phi}_a + 3H\dot{\phi}_a - \frac{1}{a^2}\nabla^2\phi_a + \frac{\partial V}{\partial\phi_a} = 0 \tag{10}$$

with $H = \dot{a}/a$.

Gravitational Waves are represented here by a transverse-traceless (TT) gauge-invariant metric perturbation, h_{ij}, on top of the flat FRW space

$$ds^2 = -dt^2 + a^2(t)\left(\delta_{ij} + h_{ij}\right)dx^i dx^j\,, \tag{11}$$

with $a(t)$ the scale factor and the tensor perturbations verifying $\partial_i h_{ij} = h_{ii} = 0$. In the following, we will raise or low indices of the metric perturbations with the delta Kronecker δ_{ij}, so $h_{ij} = h^i_j = h^{ij}$ and so on. The Einstein field equations can be splitted into the background

$G^{(0)}_{\mu\nu} = 8\pi G\, T^{(0)}_{\mu\nu}$ and the perturbed $\delta G_{\mu\nu} = 8\pi G\, \delta \mathrm{T}_{\mu\nu}$ equations. The background equations describe the evolution of the flat FRW universe through

$$-\frac{\dot{H}}{4\pi G} = \dot{\chi}^2 + \frac{1}{3a^2}(\nabla\chi)^2 + \dot{\phi}_a^2 + \frac{1}{3a^2}(\nabla\phi_a)^2 \quad (12)$$

$$\frac{3H^2}{4\pi G} = \dot{\chi}^2 + \frac{1}{a^2}(\nabla\chi)^2 + \dot{\phi}_a^2 + \frac{1}{a^2}(\nabla\phi_a)^2 + 2V(\chi,\phi) \quad (13)$$

where any term in the r.h.s. of (12) and (13), should be understood as spatially averaged.

On the other hand, the perturbed Einstein equations describe the evolution of the tensor perturbations [39] as

$$\ddot{h}_{ij} + 3H\dot{h}_{ij} - \frac{1}{a^2}\nabla^2 h_{ij} = 16\pi G\, \Pi_{ij}\,, \quad (14)$$

with $\partial_i \Pi_{ij} = \Pi_{ii} = 0$. The source of the GW, Π_{ij}, contributed by both the inflaton and the other scalar fields, will be just the transverse-traceless part of the (spatial-spatial) components of the total anisotropic stress-tensor

$$\mathrm{T}_{\mu\nu} = \frac{1}{a^2}\left[\partial_\mu\chi\partial_\nu\chi + \partial_\mu\phi_a\partial_\nu\phi_a + g_{\mu\nu}(\mathcal{L} - \langle p\rangle)\right]\,, \quad (15)$$

where $\mathcal{L}(\chi,\phi_a)$ is the lagrangian (6) and $\langle p\rangle$ is the background homogeneous pressure. As we will explain in the next subsection, when extracting the TT part of (15), the term proportional to $g_{\mu\nu}$ in the r.h.s of (15), will be dropped out from the GW equations of motion. Thus, the effective source of the GW will be just given by the TT part of the gradient terms $\partial_\mu\chi\partial_\nu\chi + \partial_\mu\phi_a\partial_\nu\phi_a$.

In summary, Eqs. (9)-(10), together with Eqs. (12)-(13), describe the coupled dynamics of reheating in any inflationary scenario, while Eq. (14) describe the production of GW in each of those scenarios. In this paper we use lattice simulations to study the generation of GW during reheating after inflation. Specific details on this are given in section IV, but let us just mention here that our approach is to solve the evolution of the gravitational waves simultaneously with the dynamics of the scalar fields, in a discretized lattice with periodic boundary conditions. We assume initial quantum fluctuations for all fields and only a zero mode for the inflaton. Moreover, we also included the GW backreaction on the scalar fields' evolution via the gradient terms, $h^{ij}\nabla_i\chi\nabla_j\chi + h^{ij}\nabla_i\phi_a\nabla_j\phi_a$ and confirmed that, for all practical purposes, these are negligible throughout GW production.

A. The Transverse-Traceless Gauge

A generic (spatial-spatial) metric perturbation δh_{ij} has six independent degrees of freedom, whose contributions can be split into scalar, vector and tensor metric perturbations [39]

$$\delta h_{ij} = \psi\,\delta_{ij} + E_{,ij} + F_{(i,j)} + h_{ij}\,. \quad (16)$$

with $\partial_i F_i = 0$ and $\partial_i h_{ij} = h_{ii} = 0$. By choosing a transverse-traceless stress-tensor source Π_{ij}, we can eliminate all the degrees of freedom (d.o.f.) but the pure TT part, h_{ij}, which represent the only physical d.o.f which propagate and carry energy out of the source (GW). If we had chosen only a traceless but non-transverse stress source, we could have eliminated the scalar d.o.f. ψ and absorbed E into the scalar field perturbation, but we would still be left with a vector field F_i also sourced by the (traceless but non-transverse) anisotropic stress tensor, thus giving rise to a vorticity divergence-less field V_i. However, since the initial conditions are those of a scalar Gaussian random field (see section IV), even in that case of a non-transverse but traceless stress source, the mean vorticity of the subsequent matter distribution, averaged over a sufficiently large volume, should be zero (although locally we do have vortices of the Higgs field, see Refs. [31, 32]), since vortices with opposite chirality cancel eachother. This means that in such a case, although $\partial^i\Pi_{ij} \neq 0$, and thus $\partial^i\delta h_{ij} \neq 0$, we could still recover the TT component when averaging over the whole realization.

For practical purposes, we will consider from the beggining the TT part of the anisotropic stress-tensor, ensuring this way that we only source the physical d.o.f. that represent GW. The equations of motion of the TT metric perturbations are then given by Eq. (14). Note that for a non-transverse source the equations would have been much more complicated, so the advantage of using the TT part from the beginning is clear. The disadvantage arises because obtaining the TT part of a tensor in configuration space is very demanding in computational time. However, as we explain next, we will use a method by which we can circunvent this issue.

Let us switch to Fourier space. Using the convention

$$f(\mathbf{k}) = \frac{1}{(2\pi)^{3/2}}\int d^3\mathbf{x}\, e^{+i\mathbf{k}\mathbf{x}} f(\mathbf{x})\,, \quad (17)$$

the GW equations (14) in Fourier space read

$$\ddot{h}_{ij}(t,\mathbf{k}) + 3H\dot{h}_{ij}(t,\mathbf{k}) + \frac{k^2}{a^2}h_{ij}(t,\mathbf{k}) = 16\pi G\,\Pi_{ij}(t,\mathbf{k})\,, \quad (18)$$

where $k = |\mathbf{k}|$. Assuming no GW at the beginnig of reheating (i.e. the end of inflation t_e), the initial conditions are $h_{ij}(t_e) = \dot{h}_{ij}(t_e) = 0$, so the solution to Eq. (18) for $t > t_e$ will be just given by a causal convolution with an appropriate green function $G(t,t')$,

$$h_{ij}(t,\mathbf{k}) = 16\pi G\int_{t_e}^{t} dt'\, G(t,t')\Pi_{ij}(t',\mathbf{k}) \quad (19)$$

Therefore, all we need to know for computing the GW is the TT part of the stress-tensor, Π_{ij}, and the Green function $G(t',t)$. However, as we will demonstrate shortly, we have used a numerical method by which we don't even need to know the actual form of $G(t',t)$. To see this, let

us extract the TT part of the total stress-tensor. Given the symmetric anisotropic stress-tensor $\mathrm{T}_{\mu\nu}$ (15), we can easily obtain the TT part of its spatial components in momentum space, $\Pi_{ij}(\mathbf{k})$. Using the spatial projection operators $P_{ij} = \delta_{ij} - \hat{k}_i\hat{k}_j$, with $\hat{k}_i = k_i/k$, then [40]

$$\Pi_{ij}(\mathbf{k}) = \Lambda_{ij,lm}(\hat{\mathbf{k}})\mathrm{T}_{lm}(\mathbf{k})\,, \tag{20}$$

where

$$\Lambda_{ij,lm}(\hat{\mathbf{k}}) \equiv \left(P_{il}(\hat{\mathbf{k}})P_{jm}(\hat{\mathbf{k}}) - \frac{1}{2}P_{ij}(\hat{\mathbf{k}})P_{lm}(\hat{\mathbf{k}})\right). \tag{21}$$

Thus, one can easily see that, at any time t, $k_i\Pi_{ij}(\hat{\mathbf{k}},t) = \Pi^i_i(\hat{\mathbf{k}},t) = 0$, as required, thanks to the identities $P_{ij}\hat{k}_j = 0$ and $P_{ij}P_{jm} = P_{im}$.

Note that the TT tensor, Π_{ij}, is just a linear combination of the components of non-traceless nor-transverse tensor T_{ij} (15), while the solution (19) is just linear in Π_{ij}. Therefore, we can write the TT tensor perturbations (i.e. the gravitational waves) as

$$h_{ij}(t,\mathbf{k}) = \Lambda_{ij,lm}(\hat{\mathbf{k}})u_{ij}(t,\mathbf{k})\,, \tag{22}$$

with $u_{ij}(t,\mathbf{k})$ the Fourier transform of the solution of the following equation

$$\ddot{u}_{ij} + 3H\dot{u}_{ij} - \frac{1}{a^2}\nabla^2 u_{ij} = 16\pi G\,\mathrm{T}_{ij} \tag{23}$$

This Eq. (23) is nothing but Eq. (14), sourced with the complete T_{ij} (15), instead of with its TT part, Π_{ij}. Of course, Eq. (23) contains unphysical (gauge) d.o.f.; however, in order to obtain the real physical TT d.o.f., h_{ij}, we can evolve Eq.(23) in configuration space, Fourier transform its solution and apply the projector (21) as in (22). This way we can obtain in momentum space, at any moment of the evolution, the physical TT d.o.f. that represent GW, h_{ij}. Whenever needed, we can Fourier transform back to configuration space and obtain the spatial distribution of the gravitational waves.

Moreover, since the second term of the r.h.s of the total stress-tensor T_{ij} is proportional to $g_{ij} = \delta_{ij} + h_{ij}$, see (15), when aplying the TT projector (21), the part with the δ_{ij} just drops out, simply because it is a pure trace, while the other part contributes with a term $-(\mathcal{L} - \langle p\rangle)h_{ij}$ in the l.h.s of Eq.(18). However, $(\mathcal{L} - \langle p\rangle)$ is of the same order as the metric perturbation $\sim \mathcal{O}(h)$, so this extra term is second order in the gravitational coupling and it can be neglected in the GW Eqs. (18). This way, the effective source in Eq. (23) is just the gradient terms of both the inflaton and the other scalar fields,

$$\mathrm{T}_{ij} = \frac{1}{a^2}\left(\nabla_i\chi\nabla_j\chi + \nabla_i\phi_a\nabla_j\phi_a\right) \tag{24}$$

Therefore, the effective source of the physical GW, will be just the TT part of (24), as we had already mentioned before.

Alternatively, one could evolve the equation of the TT tensor perturbation in configuration space, Eq. (14), with the source given by

$$\Pi_{ij}(\mathbf{x},t) = \frac{1}{(2\pi)^{3/2}}\int d^3\mathbf{k}\, e^{-i\mathbf{k}\mathbf{x}}\Lambda_{ij,lm}(\hat{\mathbf{k}})\mathrm{T}_{lm}(\mathbf{k},t)\,, \tag{25}$$

such that $\partial_i\Pi_{ij}(\mathbf{x},t) = \Pi_{ii}(\mathbf{x},t) = 0$ at any time. So, at each time step of the evolution of the fields, one would have first to compute (the gradient part of) T_{lm} (24) in configuration space, then Fourier transform it to momentum space, substitute in Eq. (25) and perform the integral. However, proceeding as we suggested above, there is no need to perform the integral, nor Fourier transform the fields at each time step, but rather only at those times at which we want to measure the GW spectrum. The viability of our method relies in the following observation. To compute the GW we could, first of all, project the TT part of the source (25), and second, solve Eq. (14). However, we achieve the same result if we commute these two operations such that, first, we solve Eq. (23), and second, we apply the TT projector to the solution (22). We have found this *commuting procedure* very useful, since we are able to extract the spectra or the spatial distribution of the GW at any desired time, saving a great amount of computing time. Most importantly, with this procedure we can take into account backreaction simultaneously with the fields evolution.

In summary, for solving the dynamics of reheating of a particular inflationary model, we evolve Eqs. (9)-(10) in the lattice, together with Eqs. (12)-(13), while for the GWs we solve Eq. (23). Then, only when required, we Fourier transform the solution of Eq. (23) and then apply (22) in order to recover the physical transverse-traceless d.o.f representing the GW. From there, one can easily build the GW spectra or take a snapshot of spatial distribution of the gravitational waves.

B. The energy density in GW

The energy-momentum tensor of the GW is given by [40]

$$t_{\mu\nu} = \frac{1}{32\pi G}\left\langle \partial_\mu h_{ij}\,\partial_\nu h^{ij}\right\rangle_{\mathrm{V}}\,, \tag{26}$$

where h_{ij} are the TT tensor perturbations solution of Eq.(14). The expectation value $\langle ...\rangle_{\mathrm{V}}$ is taken over a region of sufficiently large volume $V = L^3$ to encompass enough physical curvature to have a gauge-invariant measure of the GW energy-momentum tensor.

The GW energy density will be just $\rho_{\mathrm{GW}} = t_{00}$, so

$$\begin{aligned}\rho_{GW} &= \frac{1}{32\pi G}\frac{1}{L^3}\int d^3\mathbf{x}\,\dot{h}_{ij}(t,\mathbf{x})\dot{h}_{ij}(t,\mathbf{x}) \\ &= \frac{1}{32\pi G}\frac{1}{L^3}\int d^3\mathbf{k}\,\dot{h}_{ij}(t,\mathbf{k})\dot{h}^*_{ij}(t,\mathbf{k})\,,\end{aligned} \tag{27}$$

where in the last step we Fourier transformed each $\dot{h}_{ij}$ and used the integral definition of the Dirac delta $(2\pi)^3\delta^{(3)}(\mathbf{k}) = \int d^3\mathbf{x}\; e^{-i\mathbf{k}\mathbf{x}}$.

We can always write the scalar product in (27) in terms of the (Fourier transformed) solution u_{lm} of the Eq.(23), by just using the spatial projectors (21)

$$\dot{h}_{ij}\dot{h}_{ij} = \Lambda_{ij,lm}\Lambda_{ij,rs}\dot{u}_{lm}\dot{u}_{rs} = \Lambda_{lm,rs}\dot{u}_{lm}\dot{u}_{rs}\,, \tag{28}$$

where we have used the fact that $\Lambda_{ij,lm}\Lambda_{lm,rs} = \Lambda_{ij,rs}$. This way, we can express the GW energy density as

$$\rho_{GW} = \frac{1}{32\pi G L^3} \times \int k^2 dk \int d\Omega\, \Lambda_{ij,lm}(\hat{\mathbf{k}}) \dot{u}_{ij}(t,\mathbf{k}) \dot{u}^*_{lm}(t,\mathbf{k}). \quad (29)$$

From here, we can also compute the power spectrum per logarithmic frequency interval in GW, normalized to the critical density ρ_c, as

$$\Omega_{\rm GW} = \int \frac{df}{f}\, \Omega_{\rm GW}(f)\,, \quad (30)$$

where

$$\Omega_{gw}(k) \equiv \frac{1}{\rho_c}\frac{d\rho_{gw}}{d\log k} = \frac{k^3}{32\pi G L^3 \rho_c} \int d\Omega\, \Lambda_{ij,lm}(\hat{\mathbf{k}}) \dot{u}_{ij}(t,\mathbf{k}) \dot{u}^*_{lm}(t,\mathbf{k}) \quad (31)$$

We have checked explicitely in the simulations that the argument of the angular integral of (31) is independent of the directions in $\mathbf{k}$-space. Thus, whenever we plot the GW spectrum of any model, we will be showing the amplitude of the spectrum (per each mode k) as obtained after avaraging over all the the directions in momentum space,

$$\Omega_{gw}(k) = \frac{k^3}{8GL^3\rho_c} \left\langle \Lambda_{ij,lm}(\hat{\mathbf{k}}) \dot{u}_{ij}(t,\mathbf{k}) \dot{u}^*_{lm}(t,\mathbf{k}) \right\rangle_{4\pi} \quad (32)$$

where $\langle f \rangle_{4\pi} \equiv \frac{1}{4\pi}\int f {\rm d}\Omega$.

Finally, we must address the fact that the frequency range, for a GWB produced in the early universe, will be redshifted today. We should calculate the characteristic physical wavenumber of the present GW spectrum, which is redshifted from any time t during GW production. This is a key point, since a relatively long period of turbulence will develop after preheating, which could change the amplitude of the GWB and shift the frequency at which the spectra peaks. So let us distinguish four characteristic times: the end of inflation, t_e; the time t_* when GW production stops; the time t_r when the universe finally reheats and enters into the radiation era; and today, t_0.[1] Thus, today's frequency f_0 is related to the physical wavenumber k_t at any time t of GW production, via $f_0 = (a_t/a_0)(k_t/2\pi)$, with a_0 and a_t, the scale factor today and at the time t, respectively. Thermal equilibrium was established at some temperature T_r, at time $t_r \geq t$. The Hubble rate at that time was $M_P^2 H_r^2 = (8\pi/3)\rho_r$, with $\rho_r = g_r \pi^2 T_r^4/30$ the relativistic energy density and g_r the effective number of relativistic degrees of freedom at temperature T_r. Since then, the scale factor has increased as $a_r/a_0 = (g_{0,s}/g_{r,s})^{1/3}(T_0/T_r)$, with $g_{i,s}$ the effective entropic degrees of freedom at time t_i, and T_0 today's CMB temperature. Putting all together,

$$f_0 = \left(\frac{8\pi^3 g_r}{90}\right)^{\frac{1}{4}} \left(\frac{g_{0,s}}{g_{r,s}}\right)^{\frac{1}{3}} \frac{T_0}{\sqrt{H_r M_p}} \left(\frac{a_e}{a_r}\right) \frac{k}{2\pi}\,, \quad (33)$$

where we have used the fact that the physical wave number k_t at any time t during GW production, is related to the comoving wavenumber k through $k_t = (a_e/a_t)k$ with the normalization $a_e \equiv 1$.

From now on, we will be concerned with hybrid inflation, leaving chaotic inflation for section VI. Within the hybrid scenario, we will analyse the dependence of the shape and amplitude of the produced GWB on the scale of hybrid inflation, and more specifically on the *v.e.v.* of the Higgs field triggering the end of inflation. The initial conditions are carefully treated following the prescription adopted in paper I, as explained in section IV. Given the natural frequency at hand in hybrid models, $m = \sqrt{\lambda} v$, whose inverse m^{-1} sets the characteristic time scale during the first stages of reheating, it happens that as long as $v \ll M_p$, the Hubble rate $H \sim \sqrt{\lambda}(v^2/M_p)$ is much smaller than such a frequency, $H \ll m$. Indeed, all the initial vacuum energy ρ_0 gets typically converted into radiation in less than a Hubble time, in just a few m^{-1} time steps. Therefore, we should be able to ignore the dilution due to the expansion of the universe during the production of GW, at least during the first stages of reheating. However, as we will see, the turbulent behaviour developed after those first stages, could last for much longer than an e-fold, in which case we will have to take into account the expansion of the universe. Our approach will be first to ignore the expansion of the Universe and later see how we can account for corrections if needed. Thus, we set the scale factor $a = 1$ and the Hubble rate $H = 0$ and $\dot{H} = 0$. As we will see later, our approach of neglecting the expansion for the time of GW production, will be completely justified *a posteriori*.

The coupled evolution equations that we have to solve numerically in a lattice for the hybrid model are

$$\ddot{u}_{ij} - \nabla^2 u_{ij} = 16\pi G\, {\rm T}_{ij} \quad (34)$$

$$\ddot{\chi} - \nabla^2 \chi + \left(g^2|\phi|^2 + \mu^2\right)\chi = 0 \quad (35)$$

$$\ddot{\phi}_a - \nabla^2 \phi_a + \left(g^2\chi^2 + \lambda|\phi|^2 - m^2\right)\phi_a = 0 \quad (36)$$

with ${\rm T}_{ij}$ given by Eq.(24) with the scale factor $a = 1$. We have explicitly checked in our computer simulations that the backreaction of the gravity waves into the dynamics of both the inflaton and the Higgs fields is negligible and can be safely ignored. We thus omit the backreaction terms in the above equations.

We evaluate during the evolution of the system the mean field values, as well as the different energy components. As shown in Fig. 1, the Higgs field grows towards the true vacuum and the inflaton moves towards the minimum of its potential and oscillates around it. We have

[1] Note, however, that after thermalization there is still a small production of GW from the thermal plasma, but this can be ignored for all practical purposes.

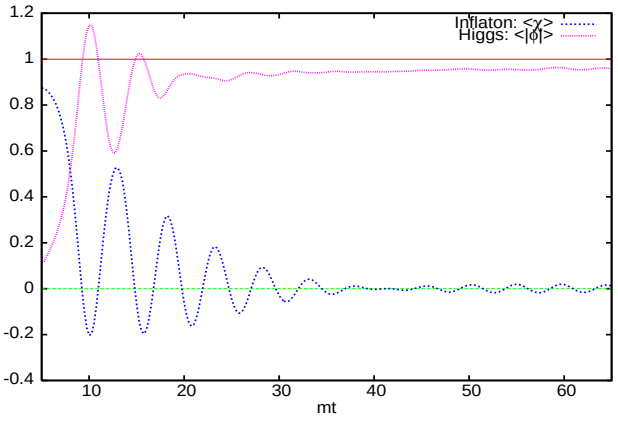

FIG. 1: Time evolution of the mean field values of the Higgs and the Inflaton, the former normalized to its *v.e.v.*, the latter normalized to its critical value $\chi_0 = \mathrm{m/g}$. This is just a specific realization with $N = 128$, $p_{\rm min} = 0.1m$, $a = 0.48m^{-1}$, $v = 10^{-3} M_p$ and $g^2 = 2\lambda = 0.25$.

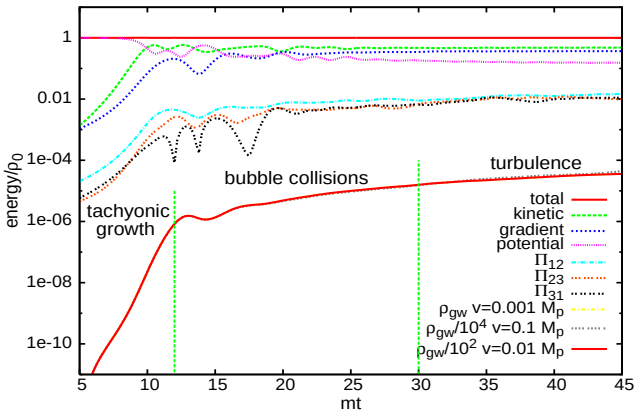

FIG. 2: The time evolution of the different types of energy (kinetic, gradient, potential, anisotropic components and gravitational waves for different lattices), normalized to the initial vacuum energy, after hybrid inflation, for a model with $v = 10^{-3}\, M_P$. One can clearly distinguish here three stages: tachyonic growth, bubble collisions and turbulence.

checked that the sum of the averaged gradient, kinetic and potential energies (contributed by both the inflaton and the Higgs), remains constant during reheating, as expected, since the expansion of the universe is irrelevant in this model. We have also checked that the time evolution of the different energy components is the same for different lattices, i.e. changing the number of points N of the lattice, of the minimum momentum $p_{\rm min} = 2\pi/L$ or of the lattice spacing $a = L/N$, with L the lattice size, as long as the product $ma < 0.5$; for a detailed discussion of lattice scales see paper I. Looking at the time evolution of the Higgs' *v.e.v.* in Fig. 1, three stages can be distinguished. First, an exponential growth of the *v.e.v.* towards the true vacuum. This is driven by the tachyonic instability of the long-wave modes of the Higgs field, that makes the spatial distribution of this field to form lumps and bubble-like structures [28, 29]. Second, the Higgs field oscillates around the true vacuum, as the Higgs' bubbles collide and scatter off eachother. Third, a period of turbulence is reached, during which the inflaton oscillates around its minimum and the Higgs sits in the true vacuum. For a detailed description of the dynamics of these fields see Ref. [29]. Here we will be only concerned with the details of the gravitational wave production.

The initial energy density at the end of hybrid inflation is given by $\rho_0 = m^2 v^2/4$, with $m^2 = \lambda v^2$, so the fractional energy density in gravitational waves is

$$\frac{\rho_{\rm GW}}{\rho_0} = \frac{4 t_{00}}{v^2\, m^2} = \frac{1}{8\pi\, G v^2 m^2} \left\langle \dot{h}_{ij} \dot{h}^{ij} \right\rangle_{\rm V} , \qquad (37)$$

where $\left\langle \dot{h}_{ij} \dot{h}^{ij} \right\rangle_V$, defined as a volume average like $\frac{1}{\rm V} \int d^3\mathbf{x} \dot{h}_{ij} \dot{h}^{ij}$, is extracted from the simulations as

$$\left\langle \dot{h}_{ij} \dot{h}^{ij} \right\rangle_{\rm V} = \\ = \frac{4\pi}{V} \int d\log k\, k^3 \left\langle \Lambda_{ij,lm}(\hat{\mathbf{k}}) \dot{u}_{ij}(t,\mathbf{k}) \dot{u}^*_{lm}(t,\mathbf{k}) \right\rangle_{4\pi} \qquad (38)$$

where $u_{ij}(t,\mathbf{k})$ is the Fourier transform of the solution of Eq. (34). Then, we can compute the corresponding density parameter today (with $\Omega_{\rm rad}\, h^2 \simeq 3.5 \times 10^{-5}$)

$$\Omega_{\rm GW}\, h^2 = \frac{\Omega_{\rm rad}\, h^2}{2G\, v^2\, m^2\, V} \times \\ \int d\log k\, k^3 \left\langle \Lambda_{ij,lm}(\hat{\mathbf{k}}) \dot{u}_{ij}(t,\mathbf{k}) \dot{u}^*_{lm}(t,\mathbf{k}) \right\rangle_{4\pi} \qquad (39)$$

which has assumed that all the vacuum energy ρ_0 gets converted into radiation, an approximation which is always valid in generic hybrid inflation models with $v \ll M_P$, and thus $H \ll m = \sqrt{\lambda}\, v$.

We have shown in Fig. 2 the evolution in time of the fraction of energy density in GW. The first (tachyonic) stage is clearly visible, with a (logarithmic) slope twice that of the anisotropic tensor Π_{ij}. Then there is a small plateau corresponding to the production of GW from bubble collisions; and finally there is the slow growth due to turbulence. In the next section we will describe in detail the most significant features appearing at each stage.

Note that in the case that $H \ll m$, the maximal production of GW occurs in less than a Hubble time, soon after symmetry breaking, while turbulence lasts several decades in time units of m^{-1}. Therefore, we can safely ignore the dilution due to the Hubble expansion, up to times much greater than those of the tachyonic instability. Eventually the universe reheats and the energy in gravitational waves redshifts like radiation thereafter.

To compute the power spectrum per logarithmic frequency interval in GW, $\Omega_{gw}(f)$, we just have to use (31). Moreover, since gravitational waves below Planck scale remain decoupled from the plasma immediately after production, we can evaluate the power spectrum today from that obtained at reheating by converting the wavenumber k into frequency f. Simply using Eq. (33), with

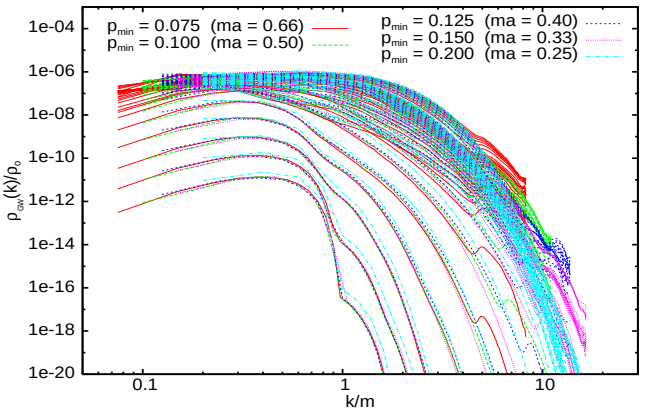

FIG. 3: We show here the comparison between the power spectrum of gravitational waves obtained with increasing lattice resolution, to prove the robustness of our method. The different realizations are characterized by the the minimum lattice momentum (p_{min}) and the lattice spacing (ma). The growth is shown in steps of $m\Delta t = 1$ up to $mt = 30$, and then in and $m\Delta t = 5$ steps up to $mt = 60$.

$g_{r,s}/g_{0,s} \sim 100$, $g_{r,s} \sim g_r$ and $a_e \sim a_*$, then

$$f = 6 \times 10^{10}\,\mathrm{Hz}\,\frac{k}{\sqrt{H\,M_p}} = 5 \times 10^{10}\,\mathrm{Hz}\,\frac{k}{m}\,\lambda^{1/4}\,. \quad (40)$$

We show in Fig. 3 the power spectrum of gravitational waves as a function of (comoving) wavenumber k/m. We have used different lattices in order to have lattice artifacts under control, specially at late times and high wavenumbers. We made sure by the choice of lattice size and spacing (i.e. $k_{\rm min}$ and $k_{\rm max}$) that all relevant scales fitted within the simulation. Note, however, that the lower bumps are lattice artifacts, due to the physical cutoff imposed at the initial condition, that rapidly disappear with time. We have also checked that the power spectrum of the scalar fields follows turbulent scaling after $mt \sim \mathcal{O}(100)$, and we can thus estimate the subsequent evolution of the energy density distributions beyond our simulations.

IV. LATTICE SIMULATIONS

The problem of determining the time evolution of a quantum field theory is an outstandingly difficult problem. In some cases only a few degrees of freedom are relevant or else perturbative techniques are applicable. However, in our particular case, our interests are focused on processes which are necessarily non-linear and non-perturbative and involve many degrees of freedom. The presence of gravitational fields just contributes with more degrees of freedom, but does not complicate matters significantly.

The lattice formulation allows a first principles approach to non-perturbative quantum field theory. The existing powerful lattice field theory numerical methods rest on the path integral formulation in Euclidean space and the existence of a probability measure in field space [41]. However, the problem we are interested in is a dynamical process far from equilibium, and the corresponding Minkowski path integral formulation is neither mathematically well founded nor appropriate for numerical studies. There are a series of alternative non-perturbative methods which different research groups have used to obtain physical results in situations similar to ours. These include Hartree's approximations [42] to go beyond perturbation theory or large N techniques [43, 44]. It is clear that it is desirable to look at this and similar problems with all available tools. In the present paper we will use an alternative approximation to deal with the problem: the classical approximation. It consists of replacing the quantum evolution of the system by its classical evolution, for which there are feasible numerical methods available. The quantum nature of the problem remains in the stochastic character of the initial conditions. This approximation has been used with great success by several groups in the past [28, 38]. The advantage of the method is that it is fully non-linear and non-perturbative, allows the use of gauge fields [31, 32] and gives access to the quantities we are interested in.

The validity of the approximation depends on the loss of quantum coherence in the evolution of the system. In previous papers we studied this problem both in the absence of and with gauge fields [29, 31, 32]. We started the evolution of the system at the critical time t_c, corresponding to the end of inflation t_e, at which the effective mass of the Higgs vanishes, putting all the modes in its (free field) ground states. If the couplings are small, since the quantum fluctuations of the value of the fields are not too large, the non-linear terms in the Hamiltonian of the system can be neglected. Then the quantum evolution is Gaussian and can be studied exactly. The Hamiltonian has nonetheless a time-dependence coming through the time-dependence of the inflaton homogeneous mode. This time dependence can always be taken to be linear for a sufficiently short time interval after the critical time. As a consequence, the dynamics of the eigenmodes during this initial phase differs significantly from mode to mode. Most of them have a characteristic harmonic oscillator behaviour with a frequency depending on the mode in question. In the case of the Higgs field, the long-wave modes become tachyonic. By looking at expectation values of products of these fields at different times, one realises that after a while these modes behave and evolve like classical modes of an exponentially growing size. The process is very fast and therefore the remaining harmonic modes can be considered to have remained in their initial ground state.

The fast growth in size of the Higgs field expectation value boosts the importance of non-linear terms and eventually drives the system into a state where the non-linear dynamics, including the back-reaction to the inflaton field, are crucial. For the whole approximation to be useful this must happen at a later time than the one

in which the low-frequency Higgs modes begin evolving as classical fields. In paper I we showed this to be the case. Actually, there is a time interval in which classical behaviour is already dominant while non-linearities are still small. We tested that our results, in the absence of gauge fields, were insensitive to the matching time, provided it lies within this window.

The whole idea can then be summarised as follows: the tachyonic quantum dynamics of the low momentum Higgs modes drive them into classical field behaviour and large occupation numbers before the non-linearities and back-reaction begin to play a role. It is the subsequent non-linear classical behaviour of the field that induces the growth of classical inflaton and gravitational field components also at low frequencies. It is obvious that the quantum nature of the problem is still crucial if one studies the behaviour of high momentum modes which have low occupation numbers.

In the present paper we apply the same idea in the presence of (gravitational wave) tensor fields. The initial quantum evolution of tensor fields is also relatively slow, since there are no tachyonic modes. Therefore, it is assumed not to affect substantially the initial conditions of the classical system.

A. Initial conditions

Our approach to the dynamics of the system is to assume that the leading effects under study can be well-described by the classical evolution of the system. The justification of this point, as explained in the previous section, rests upon the fast quantum evolution of the long wavelength components of the Higgs field during the initial stages after the critical point. All the other degrees of freedom will evolve slowly from their initial quantum vacuum state. For the Higgs field, the leading behaviour is the exponential growth of those modes having negative effective mass-squared. The quantum evolution of such modes drives the system into a quasi-classical regime. It is essential that this regime is reached before the non-linearities couple all degrees of freedom to each other and questions like back-reaction start to affect the results. It is then assumed that it is the essentially classical dynamics of that field what matters, and that all the long-wavelength components of the inflaton and the gauge fields produced by the interaction with the Higgs field behave also as classical fields. Of course, this can hardly be the case for shorter wavelengths which stay in a quantum state with low occupation numbers. However, as we can see in Fig. 3, for the range of times studied in this paper, the effect of shorter wavelengths is relatively small, and the spectrum of modes remains always dominated by long-wavelengths.

The full non-linear evolution of the system can then be studied using lattice techniques. Our approach is to discretize the classical equations of motion of all fields in both space and time. The time-like lattice spacing a_t must be smaller than the spatial one a_s for the stability of the discretized equations. In addition to the ultraviolet cut-off one must introduce an infrared cut-off by putting the system in a box with periodic boundary conditions. We have studied 64^3, 128^3 and 256^3 lattices. Computer memory and CPU resources limit us from reaching much bigger lattices. Nonetheless, in the spirit of paper I, there are a number of checks one can perform to ensure that our results are physical and are not biased, within errors, by the approximations introduced, see Fig. 3. Our problem has several physical scales which control different time-regimes and observables. Thus, it is not always an easy matter to place these scales in the window defined by our ultraviolet and infrared cut-offs. For example, in addition to the Higgs and inflaton mass there is a scale M associated to the inflaton velocity which is particularly relevant in determining the bubble sizes and collisions. Then, when we want to study a stage of the evolution in particular, we make the selection of the volume and cutoff most suitable.

Since in this paper we are more interested in understanding the phenomenon of GW production, rather than concentrating in a particular model, our attitude has been to modify the parameters of the model in order to sit in a region where our results are insensitive to the cut-offs. This is no doubt a necessary first step to determine the requirements and viability of the study of any particular model. In particular, we have thouroughly studied a model with $g^2 = 2\lambda = 1/4$, but we have checked that other values of the parameters do not change our results significantly.

The initial conditions of the fields follow the prescription from paper I. The Higgs modes ϕ_k are solutions of the coupled evolution equations, which can be rewritten as $\phi_k'' + (k^2 - \tau)\phi_k = 0$, with $\tau = M(t - t_c)$ and $M = (2V)^{1/3}m$. The time-dependent Higgs mass follows from the initial inflaton field homogeneous component, $\chi_0(t_i) = \chi_c(1 - Vm(t_i - t_c))$ and $\dot{\chi}_0(t_i) = -\chi_c Vm$. The Higgs modes with $k/M > \sqrt{\tau_i}$ are set to zero, while the rest are determined by a Gaussian random field of zero mean distributed according to the Rayleigh distribution

$$P(|\phi_k|)d|\phi_k|d\theta_k = \exp\left(-\frac{|\phi_k|^2}{\sigma_k^2}\right)\,\frac{d|\phi_k|^2}{\sigma_k^2}\,\frac{d\theta_k}{2\pi}\,, \qquad (41)$$

with a uniform random phase $\theta_k \in [0, 2\pi]$ and dispersion given by $\sigma_k^2 \equiv |f_k|^2 = P(k,\tau_i)/k^3$, where $P(k,\tau_i)$ is the power spectrum of the initial Higgs quantum fluctuations in the background of the homogeneous inflaton, computed in the linear approximation. In the region of low momentum modes it is well approximated by

$$2kP_{\rm app}(k,\tau_i) = k^3\left(1 + A(\tau_i)\,k^2\,e^{-B(\tau_i)\,k^2}\right)\,, \qquad (42)$$

where $A(\tau_i)$ and $B(\tau_i)$ are parameters extracted from a fit of this form to the exact power spectrum given in paper I. In the classical limit, the conjugate momentum $\dot{\phi}_k(\tau)$ is uniquely determined through $\dot{\phi}_k(\tau) = F(k,\tau)\phi_k(\tau)$,

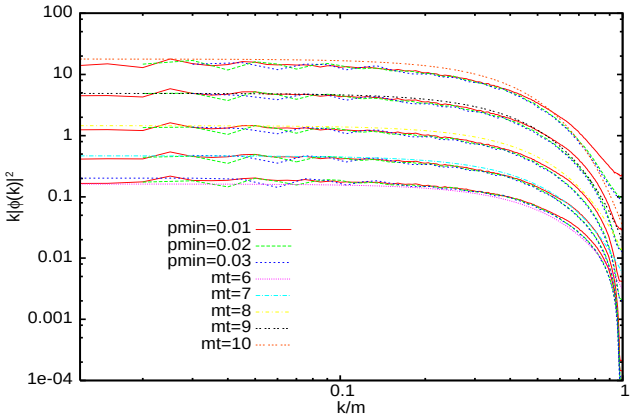

FIG. 4: The tachyonic growth of the Higgs' spectrum, from $mt = 5$ to $mt = 10$. We compare simulations of different sizes ($p_{\rm min} = 0.01 - 0.03$) and $N = 256$, with the anaylitical expressions.

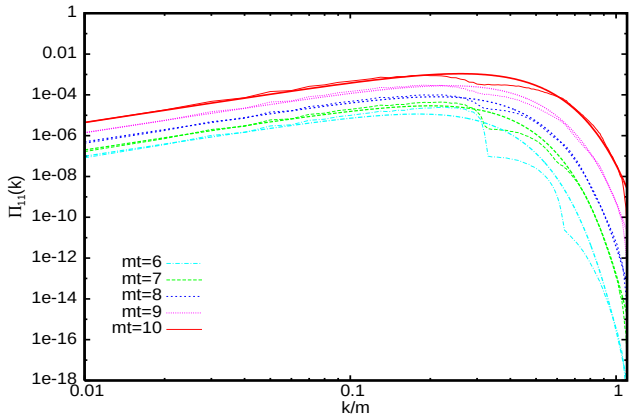

FIG. 5: The Fourier transform of the anisotropic stress tensor. We compare the numerical simulations of $\Pi_{11}(k,t)$ for $p_{\rm min} = 0.01$ with the analytical expressions (dashed lines) for $mt = 5-10$, i.e. during the tachyonic growth. The small deviations at $k \leq m$ are simulation artifacts due to the initial UV cut-off implementation and soon disappear.

where $F(k,\tau) = {\rm Im}(i f_k(\tau)\dot{f}_k^*(\tau))/|f_k(\tau)|^2$, see paper I. In the region of low momenta, $F(k,\tau_i)$ can be well aproximated by

$$F(k,\tau_i) = \frac{2kC(\tau_i)e^{-D(\tau_i)k^2}}{[1+A(\tau_i)e^{-B(\tau_i)k^2}]}. \qquad (43)$$

where $A(\tau_i)$ and $B(\tau_i)$ are the previous coefficients for the amplitude of the field fluctuations, while $C(\tau_i)$ and $D(\tau_i)$ are new coefficients obtained fitting the exact expression of $F(k,\tau_i)$.

The rest of the fields (the inflaton non-zero modes and the gravitational waves), are supposed to start from the vacuum, and therefore they are semiclassically set to zero initially in the simulations. Their coupling to the Higgs modes will drive their evolution, giving rise to a rapid (exponential) growth of the GW and inflaton modes. Their subsequent non-linear evolution will be well described by the lattice simulations.

In the next subsections we will describe the different evolution stages found in our simulations.

B. Tachyonic growth

In this subsection we will compare the analytical estimates with our numerical simulations for the initial tachyonic growth of the Higgs modes and the subsequent growth of gravitational waves. The first check is that the Higgs modes grow according to paper I. There we found that

$$k|\phi_k(t)|^2 \simeq v^2\, A(\tau)\, e^{-B(\tau)k^2}\,, \qquad (44)$$

with $A(\tau)$ and $B(\tau)$ are given in paper I,

$$A(\tau) = \frac{\pi^2(1/3)^{2/3}}{2\Gamma^2(1/3)}\,{\rm Bi}^2(\tau)\,, \qquad B(\tau) = 2(\sqrt{\tau}-1)\,, \qquad (45)$$

which are valid for $\tau > 1$, and where ${\rm Bi}(z)$ is the Airy function of the second kind. Indeed, we can see in Fig. 4 that the initial growth, from $mt = 6$ to $mt = 10$, follows precisely the analytical expression, once taken into account that in Eq. (44) the wavenumber k and time τ are given in units of $M = (2V)^{1/3}m$.

The comparison between the tensor modes $h_{ij}(k,t)$ and the numerical results is somewhat more complicated. We should first compute the effective anisotropic tensor ${\rm T}_{ij}(\mathbf{k},t)$ (24) from the gradients of the Higgs field (those of the inflaton are not relevant during the tachyonic growth), as follows,

$$\tilde{\Pi}_{ij}(\mathbf{k},t) = \int \frac{d^3\mathbf{x}\, e^{-i\mathbf{kx}}}{(2\pi)^{3/2}}\left[\nabla_i\phi^a\,\nabla_j\phi^a(\mathbf{x},t)\right]\,, \qquad (46)$$

where

$$\nabla_i\phi^a(\mathbf{x},t) = \int \frac{d^3\mathbf{q}}{(2\pi)^{3/2}}\, iq_i\,\tilde{\phi}^a(\mathbf{q},t)\, e^{-i\mathbf{qx}}\,. \qquad (47)$$

After performing the integral in $\mathbf{x}$ and using the delta function to eliminate $\mathbf{q}'$, we make a change of variables $\mathbf{q} \to \mathbf{q}+\mathbf{k}/2$, and integrate over $\mathbf{q}$, with which the Fourier transform of the anisotropic stress tensor becomes

$$\tilde{\Pi}_{ij}(\mathbf{k},t) = k_i\,k_j\,\frac{A(\tau)}{B(\tau)\sqrt{2}}\,\Psi\left[\frac{1}{2},0;\frac{B(\tau)k^2}{4}\right]\,e^{-\frac{1}{4}B(\tau)k^2}, \qquad (48)$$

which gives a very good approximation to the numerical results, see Fig. 5, with $\Psi(1/2,0;z) \simeq (\pi^{-1}+z)^{-1/2}$ being the Kummer function.

Finally, with the use of $\tilde{\Pi}_{ij}(\mathbf{k},t)$, we can compute the tensor fields,

$$h_{ij}(\mathbf{k},t) \;=\; (16\pi G)\int_0^t dt'\,\frac{\sin k(t-t')}{k}\,\tilde{\Pi}_{ij} \qquad (49)$$

$$\partial_0 h_{ij}(\mathbf{k},t) \;=\; (16\pi G)\int_0^t dt'\,\cos k(t-t')\,\tilde{\Pi}_{ij}. \qquad (50)$$

Using the analytic expression in Eq. (48) one can perform the integrals and obtain expressions that agree surprisingly well with the numerical estimates. This allows one to compute the density in gravitational waves, $\rho_{\rm GW}$, at least during the initial tachyonic stage in terms of analytical functions, and we reproduce the numerical results, see Fig. 3.

We will now compare our numerical results with the analytical estimates. The tachyonic growth is dominated by the faster than exponential growth of the Higgs modes towards the true vacuum. The (traceless) anisotropic strees tensor Π_{ij} grows rapidly to a value of order $k^2|\phi|^2 \sim 10^{-3}\, m^2 v^2$, which gives a tensor perturbation

$$\left|h_{ij}h^{ij}\right|^{1/2} \sim 16\pi G v^2 (m\Delta t)^2 10^{-3}\,, \tag{51}$$

and an energy density in GW,

$$\rho_{\rm GW}/\rho_0 \sim 64\pi G v^2\,(m\Delta t)^2 10^{-6} \sim G v^2\,, \tag{52}$$

for $m\Delta t \sim 16$. In the case at hand, with $v = 10^{-3}\, M_P$, we find $\rho_{\rm GW}/\rho_0 \sim 10^{-6}$ at symmetry breaking, which coincides with the numerical simulations at that time, see Fig. 2.

As shown in Ref. [29], the spinodal instabilities grow following the statistics of a gaussian random field, and therefore one can use the formalism of [45] to estimate the number of peaks or lumps in the Higgs spatial distribution just before symmetry breaking. As we will discuss in the next section, these lumps will give rise via non-linear growth to lump invagination and the formation of bubble-like structures with large density gradients, expanding at the speed of light and colliding among themselves giving rise to a large GWB. The size of the bubbles upon collision is essentially determined by the distance between peaks at the time of symmetry breaking, but this can be computed directly from the analysis of gaussian random fields, as performed in Ref. [29].

This analysis works only for the initial (linear) stage before symmetry breaking. Nevertheless, we expect the results to extrapolate to later times since once a bubble is formed around a peak, it remains there at a fixed distance from other bubbles. This will give us an idea of the size of the bubbles at the time of collision.

We estimate the number density of peaks as [45]

$$n_{\rm peak}(\tau) = \frac{2}{3\sqrt{3}\,\pi^2}\xi_0(\tau)^{-3}(\nu^2-1)\exp[-\nu^2/2]\,, \tag{53}$$

where $\nu = \phi_c/\sigma(\tau)$ corresponds to the ratio of the field threshold ϕ_c over the dispersion

$$\sigma(\tau) = \frac{\sqrt{\lambda}}{\pi}(2V)^{1/3}\Big(\frac{A(\tau)}{B(\tau)}\Big)^{1/2}\,, \tag{54}$$

with $A(\tau)$ and $B(\tau)$ given in Eq. (45). The average size of the gaussian lumps is $\xi_0(\tau) = 2B^{1/2}(\tau)\, m^{-1}$, where time is given in units $\tau = (2V)^{1/3}\, mt$, see Ref. [29]

The distance between peaks can be estimated as twice the radius of the average bubble, with volume $V_{\rm peak} = 4\pi/3\, R^3_{\rm peak}$. Since the total volume L^3 is divided into $N_{\rm peak}$ bubbles, we find

$$d_{\rm peak} = 2R_{\rm peak} = \frac{1}{ma}\Big(\frac{6}{\pi n_{\rm peak}}\Big)^{1/3} a, \tag{55}$$

which is typically of order 30 to 40 lattice units, for $\phi_c \simeq 0.5 - 0.8$, $V = 0.024$ and $\lambda = 0.125$, with lattices sizes given by $p_{\rm min} = 0.15\, m$ and $N = 128$.

What is interesting is that decreasing either λ or V, the distance between initial lumps increases and thus also the size of the final bubbles upon collision. As we will show in the next section, the amplitude of GW depends on the bubble size squared, and therefore it is expected that for lower lambda we should have larger GW amplitude. We have not seen, however, such an increase in amplitude, but a detailed analysis is underway and will be presented elsewhere.

C. Bubble collisions

The production of gravitational waves in the next stage proceeds through 'bubble' collisions. In Ref. [28] we showed explicitly that symmetry breaking is not at all a homogeneous process. During the breaking of the symmetry, the Higgs field develops lumps whose peaks grow up to a maximum value $|\phi|_{\rm max}/v = 4/3$ (see paper I), and then decrease creating approximately spherically symmetric bubbles, with ridges that remain above $|\phi| = v$. Finally, neighboring bubbles collide and the symmetry gets further broken through the generation of higher momentum modes. Since initially only the Higgs field sources the anisotropic stress-tensor Π_{ij}, then we expect the formation of structures (see section IV.A) in the tensor metric perturbation, correlated with the Higgs lumps. The dependence of the h_{ij} tensor on the gradient of the Higgs field, see Eq.(14), is responsible of the formation of those structures in the energy density spatial distribution of the GWB.

In section V of this paper we will give account of the explicit form of the structures developed in the spatial distribution of $\rho_{\rm GW}$ related with the first collisions among the bubble-like structures of the Higgs field. We will present simultaneously the evolution of both the Higgs' spatial distribution when the first bubbles start colliding, and of the corresponding structures in the GW energy density $\rho_{\rm GW}$. We leave for a forthcoming publication the details of an analytical formalism describing the formation and subsequent evolution of such GW structures. In this sub-section we will just give an estimate of the burst in GW produced by the first collisions of the Higgs bubble-like structures.

Thus, as described in Ref. [12] for the case of first order phase transitions, which involves the collision of vacuum bubbles, we can give a simple estimate of the order of magnitude of the energy fraction radiated in the form

of gravitational waves when two Higgs bubble-like structures collide. In general, the problem of two colliding bubbles has several time and length scales: the duration of the collision, Δt; the bubbles' radius R at the moment of the collision; and the relative speed of the bubble walls. In section IV.B we found that the typical size of bubbles upon collisions, is of the order of $R \approx 10 m^{-1}$, while the growth of the bubble's wall is relativistic. Then we can assume than the time scale associated with bubble collisions is also $\Delta t \sim R$. Assuming the bubble walls contain most of the energy density, and since they travel close to the speed of light, see paper I, it is expected that the asymmetric collisions will copiously produce GW.

Far from a source that produces gravitational radiation, the dominat contribution to the amplitude of GW is given by the acceleration of the quadrupole moment of the Higgs field distribution. Given the energy density of the Higgs field, $\rho_{\rm H}$, we can compute the (reduced) quadrupole moment of the Higgs field spatial distribution, $Q_{ij} = \int d^3x \, (x_i x_j - x^2 \delta_{ij}/3) \, \rho_{\rm H}(x)$, such that the amplitude of the gravitational radiation, in the TT gauge, is given by $h_{ij} \sim (2G/r) \ddot{Q}_{ij}$. A significant amount of energy can be emitted in the form of gravitational radiation whenever the quadrupole moment changes significantly fast: through the bubble collisions in this case. The power carried by these waves can be obtained via (29) as

$$P_{\rm GW} = \frac{G}{8\pi} \int d\Omega \left\langle \dddot{Q}_{ij} \dddot{Q}^{ij} \right\rangle . \tag{56}$$

Omitting indices for simplicity, as the power emitted in gravitational waves in the quadrupole approximation is of order $P_{\rm GW} \sim G(\dddot{Q})^2$, while the quadrupole moment is of order $Q \sim R^5 \rho_{\rm H}$, we can estimate the power emitted in GW upon the collision of two Higgs bubbles as

$$P_{\rm GW} \sim G \left(\frac{R^5 \rho}{R^3} \right)^2 \sim G \rho_{\rm H}^2 \, R^4 \tag{57}$$

The fraction of energy density carried by these waves, $\rho_{\rm GW} \sim P_{\rm GW} \Delta t / R^3 \sim P_{\rm GW}/R^2 \sim G \rho_{\rm H}^2 \, R^2$, compared to that of the initial energy stored in the two bubble-like structures of the Higgs field, will be $\rho_{\rm GW}/\rho_{\rm H} = G \rho_{\rm H} R^2$. Since the expansion of the universe is negligible during the bubble collision stage, the energy that drives inflaton, $\rho_0 \sim m^2 v^2$, is transferred essentially to the Higgs modes during preheating, within an order of magnitude, see Fig. 2. Thus, recalling that $R \sim 10 m^{-1}$, the total fraction of energy in GW produced during the bubble collisions to that stored in the Higgs lumps formed at symmetry breaking, is given by

$$\frac{\rho_{\rm GW}}{\rho_0} \sim 0.1 \, G \rho_0 \, R^2 \sim (v/M_p)^2 \, , \tag{58}$$

giving an amplitude which is of the same order as is observed in the numerical simulations, see Fig. 2. Of course, an exhaustive analytical treatment of the production of GW during this stage of bubble collisions remains to be done, but we leave it for a future publication.

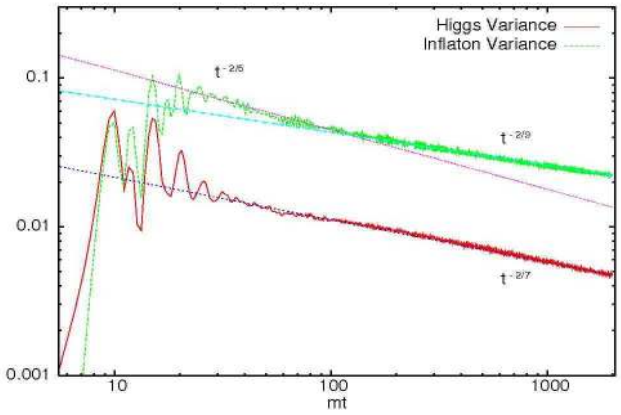

FIG. 6: Variance of the Inflaton and the Higgs field as a function of time, the former normalized to its critical value, the latter normalized to its *v.e.v.*. As expected in a turbulent regime, these variances follow a power law $\sim t^{-2p}$ with p a certain critical exponent, although the slope of the Inflaton's variances evolves in time. The curves are produced from an average over 10 different statistical realizations.

D. Turbulence

The development of a turbulent stage is expected from the point of view of classical fields, as turbulence usually appears whenever there exists an active (stationary) source of energy localized at some scale $k_{\rm in}$ in Fourier space. As first pointed out by Ref. [46], in reheating scenarios the coherently oscillating inflaton zero-mode plays the role of the pumping-energy source, acting at a well defined scale $k_{\rm in}$ in Fourier space, given by the frequency of the inflaton oscillations. Thus, the inflaton zero-mode pumps energy into the rest of the fields that couple to it as well as into the non-zero modes of the inflaton field itself. Apart from $k_{\rm in}$, there is no other scale in Fourier space where energy is accummulated, dissipated and/or infused. So, as turbulence is characterized by the transport of some conserved quantity, energy in our case, we should expect a flow of energy from $k_{\rm in}$ towards higher (direct cascade) or smaller (inverse cascade) momentum modes. In typical turbulent regimes of classical fluids, there exits a sink in Fourier space, corresponding to that scale at which the (direct) cascade stops and energy gets dissipated. However, in our problem there is no such sink so that the transported energy cannot be dissipated, but instead it is used to populate high-momentum modes. For the problem at hand, there exists a natural initial cut-off $k_{\rm out} \sim \lambda^{1/2} v$, such that only long wave modes within $k < k_{\rm out}$, develop the spinodal instability. Eventually, after the tachyonic growth has ended and the first Higgs' bubble-like structures have collided, the turbulent regime is established. Then the energy flows from small to greater scales in Fourier space, which translates into the increase of $k_{\rm out}$ in time.

In Ref. [32] we already accounted for the turbulent stage reached in a hybrid model with gauge fields. However, we don't consider gauge fields here, so the number

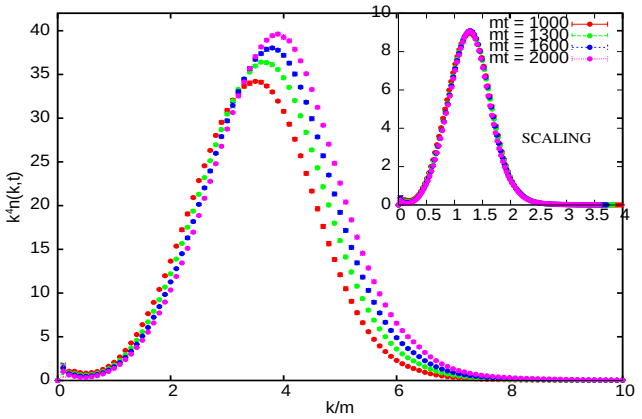

FIG. 7: Some snapshots of the evolution of the spectral particle occupation numbers of the Higgs field at different times, each averaged over 10 statistical realizations. We multiply them by k^4 so we can see better the scaling behaviour. In the upper right corner, we plot the inverse relation of (60), $n_0(kt^{-p}) = t^{\gamma p} n(k,t)$, also averaged over 10 realizations for each time. The scaling behaviour predicted by wave kinetic turbulent theory [46], is clearly verified.

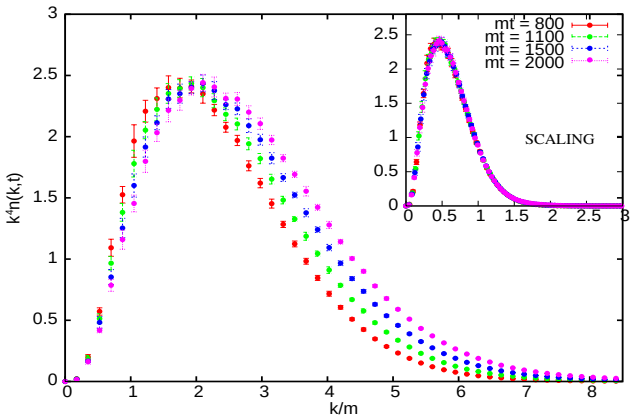

FIG. 8: Different times of the evolution of the particle occupation numbers spectra of the Inflaton, multiplied by k^4, and averaged over 10 statistical realizations or each time. Again, in the upper right corner, we plot the inverse relation of (60), $n_0(k) = t^{\gamma p} n(kt^p, t)$, also averaged over 10 realizations for each time.

of degrees of freedom is different from that of Ref. [32] and, therefore, the turbulent dynamics of the Inflaton and the Higgs fields should be different. In particular, when the turbulence has been fully established, if the wave (kinetic) turbulence regime of the fields' dynamics is valid, the time evolution of the variance of a turbulent field $f(\mathbf{x}, t)$, should follow a power-law-like scaling [46]

$$\mathrm{Var}(f(t)) = \langle f(t)^2 \rangle - \langle f(t) \rangle^2 \propto t^{-2p}\,, \tag{59}$$

with $p = 1/(2N-1)$ and N the number of scattering fields in a 'point-like collision'. In fact, such time behaviour corresponds only to the case of the so called *free turbulence*, when the energy stored in the pumping source is subdominant to the energy in the turbulent fields. In our case, this condition is reached very soon after the symmetry breaking, so we don't expect a significant stage of *driven turbulence*, which would make the variance to increase (Only the inflaton seems to increase its variance between $mt = 10$ and $mt = 30$, but it is not very pronounced). In Fig. 6 we have plotted the time evolution of the variances of the Inflaton χ and of the Higgs modulus $\phi = \sqrt{\sum_a \phi_a^2}$, and fitted the data with a power-law like (59), obtaining

$$\begin{aligned} \text{Inflaton: } p_{_I}^{-1} &= 5.1 \pm 0.2, \quad [35{:}85] \\ \text{Inflaton: } p_{_I}^{-1} &= 9.03 \pm 0.03, \quad [350{:}2000] \\ \text{Higgs: } p_{_H}^{-1} &= 7.02 \pm 0.01, \quad [50{:}2000] \end{aligned}$$

where the last brackets on the right correspond to the range in time (in units of m^{-1}) for which we fitted the data. As can be seen in Fig. 6, the slope of the Higgs field (in logarithmic scale), $2p_{_H} \sim 2/7$, remains approximately constant in time, corresponding to a 4-field dominant interaction. However, the slope of the Inflaton's variance increases in time, i.e. the critical exponent $p_{_I}$ of the Inflaton decreases, until it reaches a stationary stage at $mt \sim 100$. Since $p_{_I}$ is related to the number N of fields interacting in a collision, if there was a change from one dominant multi-field interaction to another, this should produce a time-dependent effective $p_{_I}$, as seen in Fig. 6. However, we will not try to explain here the origin of such an effective critical exponents as extracted from the simulations. We will just stress that we have checked the robustness of those values under different lattice configurations $(N, p_{\rm min})$ and different statistical realizations, discarding this way a possible lattice artefact effect. As we will see, the critical exponents p determines the speed with which the turbulent particle distribution moves over momentum space, so this is a crucial parameter. Moreover, although both the classical modes of the Inflaton and the Higgs contribute to the production of GW, the Inflaton's occupation numbers decrease faster than those of the Higgs so, after a given time, only the Higgs' modes remain as the main source of GW.

Actually, when turbulence is developed, it is expected that the distribution function of the classical turbulent fields, the inflaton and the Higgs here, follow a self-similar evolution [46]

$$n(k,t) = t^{-\gamma\, p} n_0(k\, t^{-p}) \tag{60}$$

with p the critical exponent of the fields' variances and γ a certain factor $\sim O(1)$, which depends on the type of turbulence developed. It is precisely this way that the exponent p determines the speed of the particles' distribution in momentum space: given a specific scale k_c such that, for example, the occupation number has a maximum, that scale evolves in time as $k_c(t) = k_c(t_0)(t/t_0)^p$. We have seen that the evolution of the Higgs occupation number follows Eq. (60) with $p \approx 1/7$, as expected from the Higgs variance, and $\gamma \approx 2.7$. Whereas the evolution of the Inflaton occupation number follows (60) even more accurately than the Higgs, with an "effective" exponent $p \approx 1/5$, and $\gamma \approx 3.9$. Since the slope of the inflaton's variance changes in time, the value of the exponents of

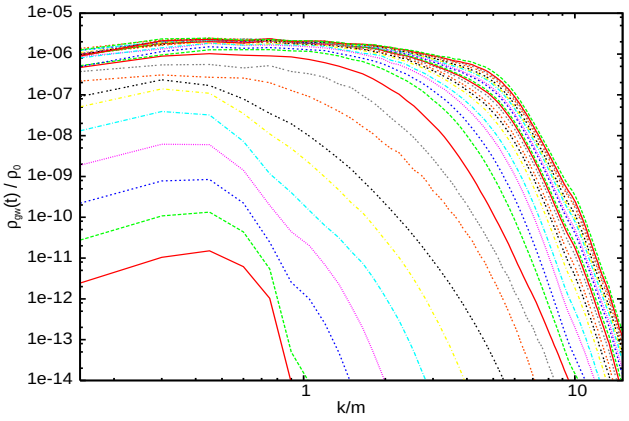

FIG. 9: Time evolution of the GW spectra from mt = 6 to mt = 2000. The amplitude of the spectra seems to saturate after mt $\sim$ 100, although the high momentum tail still moves slowly to higher values of k during the turbulent stage.

the inflaton's scaling relation will require further investigation. However, despite this time evolution of the Inflaton variance, Eq. (60) is very well fulfilled by the Inflaton with the given effective exponents. So we can perfectly obtain the universal $n_0(k)$ function for the Inflaton as well as for the Higgs.

In Figs. 7 and 8 we have plotted the occupation numbers of the Higgs and the Inflaton, also inverting the relation of Eq. (60) in order to extract the *universal* time-independent $n_0(k)$ functions of each field. As shown in those figures, the distributions follow the expected scaling behaviour. However, for the range of interest of k, there are small discrepancies of order 0.1-4% (depending on k) among the different universal functions $n_0^{(i)}(k)$, as obtained inverting Eq. (60) at different times mt_i. The universal functions $n_0(k)$ plotted in Figs. 7 and 8 have been obtained from averaging over ten statistical realizations for each time.

The advantage of the development of a turbulence behaviour is obvious: it allows us to extrapolate the time evolution of the fields' distributions till later times beyond the one we can reach with the simulations. Moreover, the fact that the turbulence develops so early after the tachyonic instability, also allow us to check for a long time of the simulation, the goodness of the description of the dynamics of the fields, given by the turbulent kinetic theory developed in Ref. [46]. We have fitted the averaged universal functions $n_0(k)$ with expressions of the form $k^4\, n_0(k) = P(k)e^{-Q(k)}$, with $P(k)$ and $Q(k)$ polynomials in k, giving:

$$\begin{aligned} &\text{Inflaton}: \quad P(k) = 486.2k^3 \quad Q(k) = 6.39k \\ &\text{Higgs}: \quad\;\; P(k) = 2.96k^3 \quad Q(k) = 2.26k^2 - 3.18k \end{aligned} \tag{61}$$

There is no fundamental meaning for these expressions, but it is very useful to have such an analytical control over $n_0(k)$, since this allows us to track the time-evolution of $n(k,t)$ through Eq. (60). Actually, the classical regime of the evolution of some bosonic fields ends when the system can be relaxed to the Bose-Einstein distribution. We are now going to estimate the moment in which the initial energy density gets fully transferred to the Higgs classical modes. Using Eq.(60) and the fit (61), we find that the initial energy density is totally transfered to the Higgs when (in units $m = 1$)

$$\rho_0 = \frac{1}{4\lambda} = \int \frac{dk}{k}\, \frac{k^3}{2\pi^2}\, k\, n(k,t) = \frac{7.565}{2\pi^2}\, t^{(4-\gamma)p}\,, \tag{62}$$

where we have assumed that the Higgs' modes have energy $E_k(k,t) = k\, n(k,t)$. In our case, with $\lambda = 1/8$, the conversion of the initial energy density into Higgs particles and therefore into radiation is complete by $mt \sim 6 \times 10^4$. Therefore, if we consider this value as a lower bound for the time that classical turbulence requires to end, we see that turbulence last for a very long time compared to the time-scale of the initial tachyonic and bubbly stages. Thus, if GW were significatively sourced during turbulence, one should take into account corrections from the expansion of the universe.

In Fig. 9, we show the evolution of the GW spectra up to times mt = 2000, for a lattice of (N,$p_{\rm min}$) = (128,.15). It is clear from that figure that the amplitude of the GW saturates to a value of order $\rho_{gw}/\rho_0 \approx 2 \cdot 10^{-6}$. At mt $\approx$ 50, the maximum amplitude of the spectra has already reached $\rho_{gw}/\rho_0 \approx 10^{-6}$, while at time mt $\approx$ 100, the maximum has only grown a factor of 2 with respect to mt $\approx$ 50. From times mt $\approx$ 150 till the maximum time we reached in the simulations, mt = 2000, the maximum of the amplitude of the spectrum does not seem to change significantly, slowly increasing from $\approx 2 \cdot 10^{-6}$ to $\approx 2.5 \cdot 10^{-6}$. Despite this saturation, we see in the simulations that the the long momentum tail of the spectrum keeps moving towards greater values. This displacement is precisely what one would expect from turbulence, although it is clear that the amplitude of the new high momentum modes never exceed that of lower momentum. In order to disscard that this displacement towards the UV is not a numerical artefact, one should further investigate the role played by the turbulent scalar fields as a source of GW. Here, we just want to remark that the turbulent motions of the scalar fields, seem not to increase significatively anymore the total amplitude of the GW spectrum. Indeed, in a recent paper [25] where GW production at reheating is also considered, it is stated that GW production from turbulent motion of classical scalar fields, should be very supressed. That is apparently what we observe in our simulations although, as pointed above, this issue should be investigated in a more detailed way. Anyway, here we can conclude that the expansion of the Universe during reheating in these hybrid models, does not play an important role during the time of GW production, and therefore we can be safely ignore it.

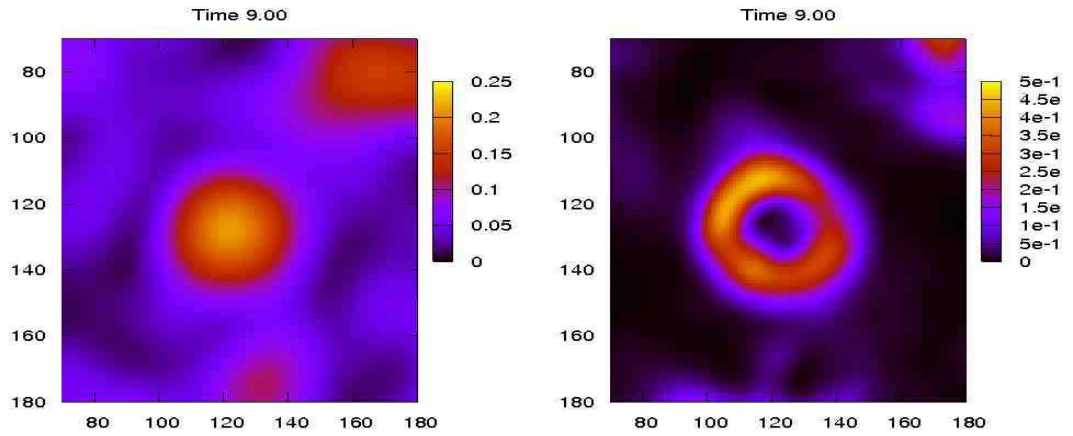

FIG. 10: Model: $\lambda = 10^{-3}$, $g^2 = 1$. In the left picture we show a spatial section of $\langle\phi\rangle$. We can see how a spherical lump is growhing. In the right picture we can see the structure of the ρ_{GW} in the same place. A ring is forming around the Higgs lump. More complex structures are formed in the regions in which the Higgs bubbles are next, and the GW grow in the boundary of this lumps, where the gradient of the Higgs and therefore the Π_{ij} tensor grow in this region.

V. SPATIAL SECTIONS AND LOCAL GW PRODUCTION

In this section, we show a sequence of snapshots ($mt = 5 - 20$) of the evolution of the spatial distribution, before the fields are driven to the turbulent stage. We find that the first stages of the GW dynamics is strongly correlated with the dynamics of the Higgs oscillations that give rise to symmetry breaking. A qualitative way of understanding this question is to analyse the spatial structure of the Π_{ij} tensor, built from spatial gradients of the Higgs and inflaton fields. Since the oscillations of $\langle\phi\rangle$ are due to rapid changes of the Higgs' values in its way of symmetry breaking, this induces great variations in the behaviour of the spatial gradients. We are now going to analyse briefly the different stages showing the most representatives images. Shortly, it will be available in our web page, a bigger selection of pictures and movies [47].

An interesting conclusion from the set of Figs. $10 - 14$ is that the Higgs evolution from lump growth, through invagination to bubble collisions, has a direct translation into the corresponding growth of gravitational wave energy density. Not only does the volume-averaged amplitude $\rho_{\rm GW}$ follow the Higgs time evolution, but the individual local features in the GWB seem to correspond very closely with the Higgs features.

In the first stage both Higgs and GW backgrounds grow very fast. The lumps which grow in the Higgs background induce structures around these, through the gradients appearing in the Π_{ij} tensor. The geometry of the gravitational structures comes from the position of the Higgs lump. A typical structure for an isolated lump is a ring of gravitational waves, see Fig. 10. More complex structures can be formed around the position of the Higgs lumps. Before symmetry breaking these lumps grow according to the previous analysis, generating domains with a great density of gravitational energy.

The second stage begins when $\langle\phi\rangle = v$ and the symmetry breaking starts, then the Higgs lumps invaginate and expand, producing the growth of gravitational waves around of these structures, see Figs. 11 and 12, one can see that whenever the bubble walls expand, the variation in the gradient of the Higgs' field induces the expansion of the GW ring. In the case of the rings, if the lump is very isolated, the expansion induces the ring to dilute and disappear, by Gauss law. In practice, however, the lumps are never isolated and bubbles collide before the gradients (and thus the GW) die away.

In the case when two Higgs' bubble-like structures are close by, the expansion of their walls compresses the GW structures. This expansion continues until the first Higgs oscillation, see Fig. 3. If the distance between Higgs' structures is small, then the GW can be diluted, whereas in the other case, a remnant string-like GW structure survives, and when the Higgs background goes to zero this GW structure becomes divided into two waves that propagate in opposite directions, as one can see in Figs. 13 and 14, which show four snapshots of this process. A similar behaviour is observed in the second oscillations.

Finally, the wave fronts propagate, colliding among themselves, driving the system to the stage of turbulence. We will leave for a future publication the detailed analysis of the GW production at the bubble collisions and the subsequent turbulent period.

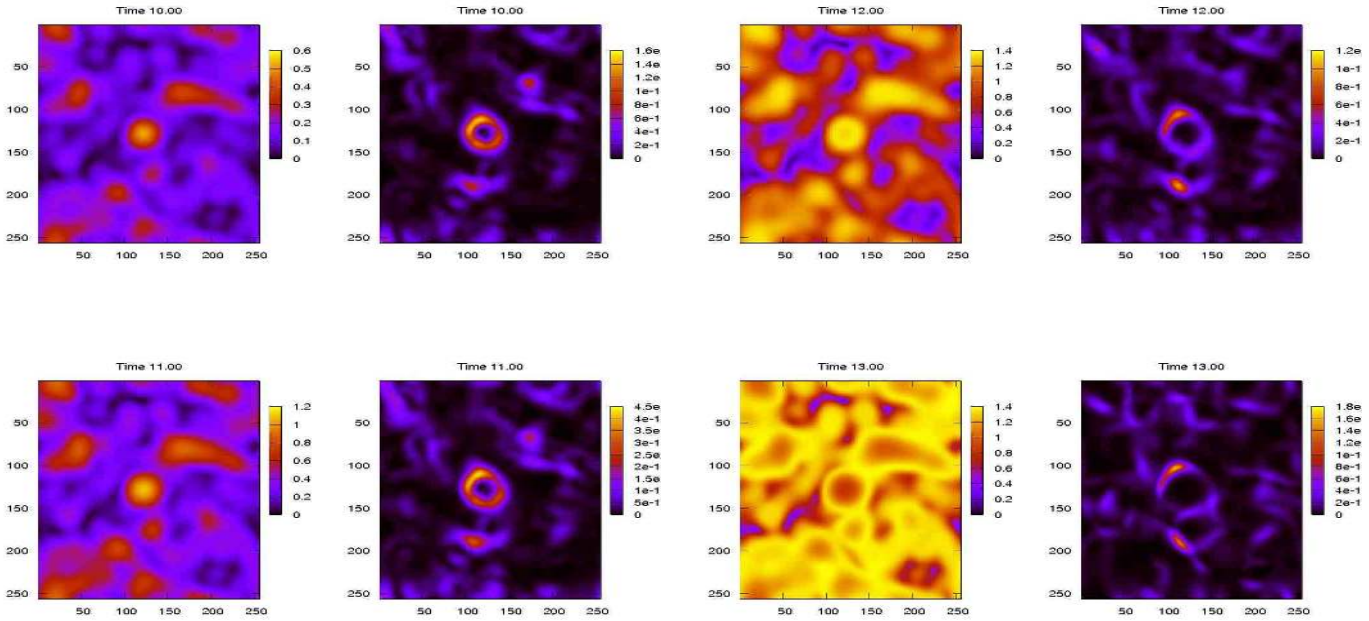

FIG. 11: Here we have got the time evolution of the previous ring (picture 10) near the symmetry breaking. The bubble is growing (mt = 10-11), until the symmetry breaking time (mt = 12).

FIG. 12: The Higgs lump begins to invaginate, and the GW ring expands (mt = 12-13). A similar behavior is observed in a smaller lump below the biggest Higgs lump, in the same pictures.

VI. GRAVITATIONAL WAVES FROM CHAOTIC INFLATION

The production of a relic GWB at reheating was first addressed by Khlebnikov and Tkachev (KT) in Ref. [21], both for the quadratic and quartic chaotic inflation scenarios. In these models, the long-wavelength part of the spectrum is dominated by the gravitational bremsstrahlung associated with the scattering of the extra scalar particles off the inflaton condensate, 'evaporating' this way the inflaton particles. Using this fact, KT estimated analytically the amplitude of the power spectra of GW for the low frequency end of the spectrum, corresponding to wavelengths of order the size of the horizon at rescattering. Moreover, KT also studied the GW power spectra numerically, although just for the massless inflaton case. Recently, chaotic scenarios were revisited in Ref. [23, 24], accompanied by more precise numerical simulations at different energy scales, including the case of a massive inflaton. Finally, also very recently, Ref. [25] studied in a very detailed way, both analitical and numerically, the evolution of GW produced at preheating in the case of a massless inflaton with an extra scalar field.

In Refs. [21] and [23], the procedure to compute the GW from reheating relied on Weinberg's formula for the energy carried by a weak gravitational radiative field in flat space-time [48]. However, in chaotic models, the expansion of the universe can not be neglected during reheating, so Weinberg's formula can only be used in an approximated way, if the evolution of the universe is considered as an adiabatic sequence of stationary universes. Rescaling fields by a conformal transformation, their evolution equations can be solved with a numerical integrator, while the evolution of the scale factor can be calculated analytically. Discretizing the time, the physical variables can be recovered from the conformal ones in each time step, thus allowing to compute the energy of gravitational waves in terms of the physical fields. In this paper, however, we adopt another approach[2] that takes into account expansion of the universe in a self-consistent manner, and let us calculate at any time the energy density and power spectra of the GW produced at reheating. As explained in section III and applied to the case of hybrid inflation in sections IV and V, we just solve numerically Eq. (23), together with those eqs. of the other Bose fields and the scale factor, Eqs. (9),(10) and Eqs.(12),(13). Then, using the projector (21) into

[2] Note that Refs. [24] and [25] also work in the same theoretical framework, considering the TT tensor perturbations on top of a flat FRW space. However, we use a different way to extract numerically the GW power spectra, relying on the *conmutating procedure*, as detailed explained in subsection III.B

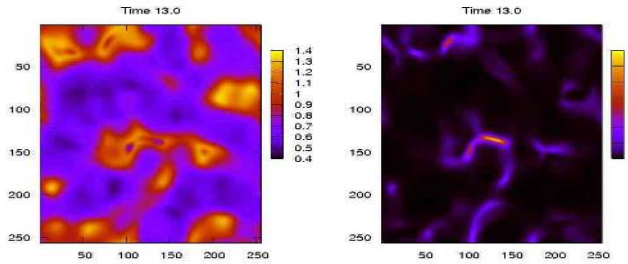

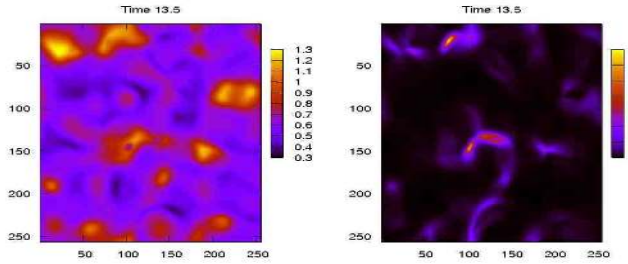

FIG. 13: After symmetry breaking the expansion of Higgs lump compresses the GW, until the Higgs gradient changes in the first oscillation (mt =13-13.5).

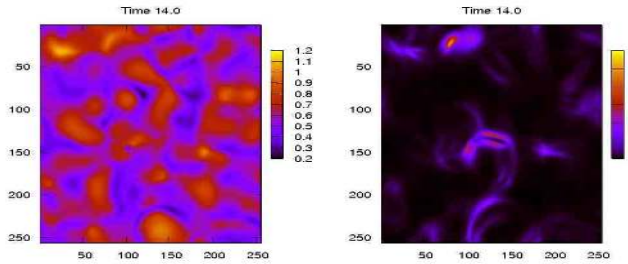

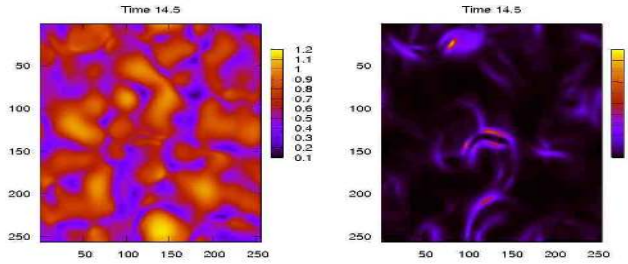

FIG. 14: At this moment, when the Higgs falls, the GW strutrure is divided in two waves (mt = 14). These wave fronts propagates in opposite directions (mt = 14.5).

the (Fourier transformed) solution of Eq.(23), we recover the TT d.o.f corresponding to GW. This way, we can monitor the total energy density in GW using Eq. (29), or track the evolution of the power spectrum. Using this technique, we will show in this section that we reproduce, for specific chaotic models, similar results to those of other authors.

We adapted the publicly available LATTICEEASY code [35], taking advantage of the structure of the code itself, incorparating the evolution of Eq. (14), together with the equations of the scalar fields, Eqs. (9) and (10), into the staggered leapfrog integrator routine. This way, we can solve at the same time the dynamics of the scalar and tensor fields, within the framework of an expanding FRW universe Eqs.(12) and (13).

In particular, we will concentrate only in an scenario with a massless inflaton χ, either accompanied or not by an extra scalar field ϕ. In the following, we will describe the numerical results for GW production at reheating in such scenarios, described by the potential

$$V(\chi,\phi) = \frac{\lambda}{4}\chi^4 + \frac{1}{2}g^2\chi^2\phi^2 \tag{63}$$

Rescaling the time by

$$d\tau = \frac{a(\tau)}{a(0)}\chi(0)\sqrt{\lambda}\,dt\,, \tag{64}$$

and the physical fields by a conformal transformation as

$$\chi_c(\tau) = \frac{a(\tau)}{a(0)}\frac{\chi(\tau)}{\chi(0)}\,, \tag{65}$$

$$\phi_c(\tau) = \frac{a(\tau)}{a(0)}\frac{\phi(\tau)}{\chi(0)} \tag{66}$$

then the equations of motion of the inflaton and of the extra scalar field, Eqs. (9) and (10), can be rewritten in terms of the conformal variables as

$$\chi_c'' - \nabla^2\chi_c - \frac{a''}{a}\chi_c + (\chi_c^2 + q\phi_c^2)\chi_c = 0 \tag{67}$$

$$\phi_c'' - \nabla^2\phi_c - \frac{a''}{a}\chi_c + q\chi_c^2\phi_c = 0\,, \tag{68}$$

where the prime denotes derivative with respect to conformal time. Since the universe expands as radiation-like in these scenarios, $a(\tau) \sim \tau$, so the terms proportional to a''/a in Eqs. (67) and (68) are soon zero, as explicitly checked in the simulations. Thanks to this, the model is conformal to Minkowski.

The parameter $q \equiv g^2/\lambda$ controls the strength and width of the resonance. For the case of a massless inflaton without an extra scalar field, we just set $q = 0$ in Eq. (67) and ignore Eq. (68). However, in that case, fluctuations of the inflaton also grow via parametric resonance. Actually, they grow as if they were fluctuations of a scalar field coupled to the zero-mode of the inflaton with effective couplig $q = g^2/\lambda = 3$, see Ref. [49].

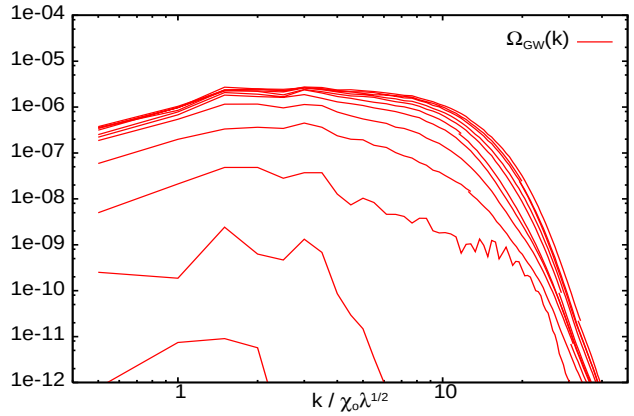

FIG. 15: The spectrum of the gravitational waves' energy density, for coupled case with $\lambda = 10^{-14}$ and $g^2/\lambda = 120$. The spectrum is shown accumulated up to different times during GW production, so one can see its evolution. At each time, it is normalized to the total instant density. This plot corresponds to a N = 128 lattice simulation, from $\tau = 0$ to $\tau = 240$.

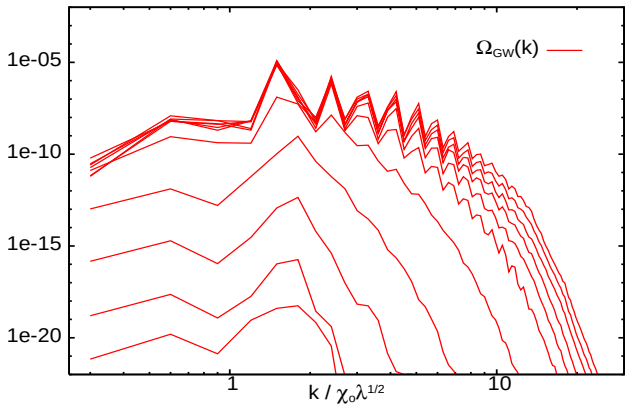

FIG. 16: The spectrum of the gravitational waves' energy density, for the pure case, with $\lambda = 10^{-14}$. Again, we show the spectrum accumulated up to different times during GW production, normalized to the total instant density at each time. The plot corresponds to a N = 128 lattice simulation, from $\tau = 0$ to $\tau = 2000$.

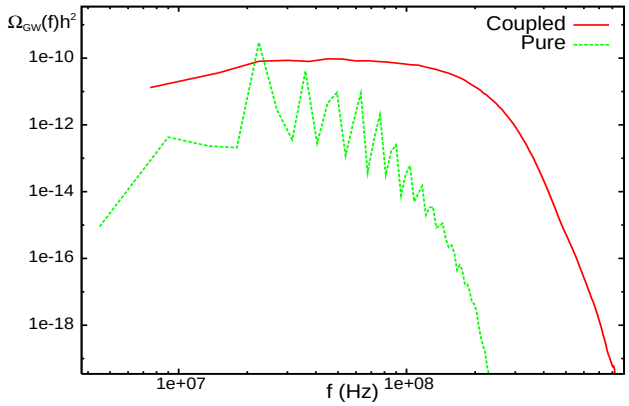

FIG. 17: Today's ratio of gravitational waves normalized to radiation energy density, for both the coupled and the pure case. We took $g_*/g_0 = 100$ to redshift the spectra from the time of the end of production till today.

Following Refs. [21] and [23], we set $\lambda = 10^{-14}$ and $q = 120$. Since, this case is also computed in [25], we can also compare our results with theirs. Moreover, we also present results for the pure $\lambda\chi^4$ model with no extra scalar field, a case only shown in Ref. [21].

We begin our simulations at the end of inflation, when the homogeneous inflaton verifies $\chi_0 \approx 0.342 M_p$ and $\dot{\chi}_0 \approx 0$. We took initial quantum (conformal) fluctuations $1/\sqrt{2k}$ for all the modes up to a certain cut-off, and only added an initial zero-mode for the inflaton, $\chi_c(0) = 1$, $\chi_c(0)' = 0$. In Figs. 15 and 16, we show the evolution of Ω_{GW} during reheating, normalized to the instant density at each time step, for the coupled and the pure case, respectively. In the case with an extra scalar field, the amplitude of the GWB saturates at the end of parametric resonance, when the fields variances have been stabilized. This is the beginnig of the turbulent stage in the scalar fields, which seems not to source anymore the production of GWs, as already stated in Refs.[23, 25]. For the pure case, we also see the saturation of the amplitude of the spectra, see Fig. 16, although the long momenta tail seems to slightly move toward higher values.

Of course, in either case, with and without an extra field ϕ, in order to predict today's spectral window of the GW spectrum, we have, first, to normalize their energy density at the end of GW production to the total energy density at that moment. Secondly, we have to redshift the GW spectra from that moment of reheating, taking into account that the rate of expansion have changed significantly since the end of inflation, see Eq.(33). In particular, the shape and amplitude of GW spectra for the case with the extra scalar field coupled to the inflaton with $q = 120$, see Fig. 17, seems to coincide with the espectra shown in Ref. [25]. On the other hand, we also reproduce in Fig. 17 a similar spectra to the one shown in [21], for the case of the pure quartic model. Thanks to the tremendous gain in computer power, we were able to resolve the 'spiky' pattern of the spectrum with great resolution. For the first time, it is clearly observed the exponential tail for large frequencies, see Figs. 16, 17, not shown in Ref. [21]. The most remarkable fact, is that we also confirm that the peak structure in the GW power spectrum, see Fig. 16, remains clearly visible at times much later than the one at which those peaks have dissapeared in the scalar fields' power spectrum. So, as pointed out in Ref. [21], this characteristic feature distinguish this particular model from any other.

Let us emphasize that we have run the simulations till times much greater than that of the end of the resonance stage, both for the pure and the coupled case. The role of the turbulence period after preheating seems, therefore, not to be very important, despite its long duration. Apparently, the *no-go* theorem about the suppresion of GW at turbulence, discussed in [25], is fulfilled. In Refs. [31, 51] it was pointed out that gauge couplings

or trilinear interactions could be responsible for a fast thermalization of the universe after inflation (see also Ref. [52]), but as long as this takes place after the end of the resonace stage, in principle this should not affect the results shown above.

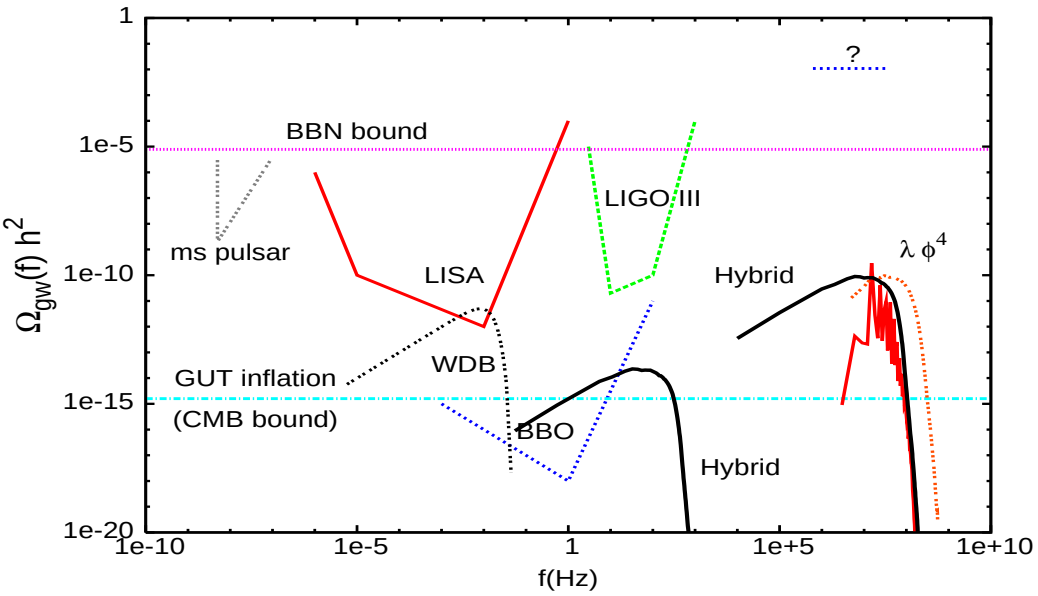

FIG. 18: The sensitivity of the different gravitational wave experiments, present and future, compared with the possible stochastic backgrounds; we include the White Dwarf Binaries (WDB) [50] and chaotic preheating ($\lambda\phi^4$, coupled and pure) for comparison. Note the two well differentiated backgrounds from high-scale and low-scale hybrid inflation. The bound marked (?) is estimated from ultra high frequency laser interferometers' expectations [15].

VII. CONCLUSIONS

To summarize, we have shown that hybrid models are very efficient generators of gravitational waves at preheating, in three well defined stages, first via the tachyonic growth of Higgs modes, whose gradients act as sources of gravity waves; then via the collisions of highly relativistic bubble-like structures with large amounts of energy density, and finally via the turbulent regime (although this effect does not seem to be very significant in the presence of scalar sources), which drives the system towards thermalization. These waves remain decoupled since the moment of their production, and thus the predicted amplitude and shape of the gravitational wave spectrum today can be used as a probe of the reheating period in the very early universe. The characteristic spectrum can be used to distinguish between this stochastic background and others, like those arising from NS-NS and BH-BH coalescence, which are decreasing with frequency, or those arising from inflation, that are flat [53].

We have plotted in Fig. 18 the sensitivity of planned GW interferometers like LIGO, LISA and BBO, together with the present bounds from CMB anisotropies (GUT inflation), from Big Bang Nucleosynthesis (BBN) and from milisecond pulsars (ms pulsar). Also shown are the expected stochastic backgrounds of chaotic inflation models like $\lambda\phi^4$, both coupled and pure, as well as the predicted background from two different hybrid inflation models, a high-scale model, with $v = 10^{-3}M_P$ and $\lambda \sim g^2 \sim 0.1$, and a low-scale model, with $v = 10^{-5}M_P$ and $\lambda \sim g^2 \sim 10^{-14}$, corresponding to a rate of expansion $H \sim 100$ GeV. The high-scale hybrid model produces typically as much gravitational waves from preheating as the chaotic inflation models. The advantage of low-scale hybrid models of inflation is that the background produced is within reach of future GW detectors like BBO [6]. It is speculated that future high frequency laser interferometers could be sensitive to a GWB in the MHz region [15], although they are still far from the bound marked with an interrogation sign.

For a high-scale model of inflation, we may never see the predicted GW background coming from preheating, in spite of its large amplitude, because it appears at very high frequencies, where no detector has yet shown to be sufficiently sensitive. On the other hand, if inflation occured at low scales, even though we will never have a chance to detect the GW produced during inflation in the polarization anisotropies of the CMB, we do expect gravitational waves from preheating to contribute with an important background in sensitive detectors like BBO. The detection and characterization of such a GW background, coming from the complicated and mostly unknown epoch of rehating of the universe, may open a new window into the very early universe, while providing a new test on inflationary cosmology.

Acknowledgments

We wish to thank Andrés Díaz-Gil, Jean-Francois Dufaux, Richard Easther, Gary Felder, Margarita García Pérez, John T. Giblin Jr., Seiji Kawamura, Lev Kofman, Andrei Linde, Eugene A. Lim, Luis Fernando Muñoz-Mejías and Mischa Sallé for very useful comments, suggestions and constructive criticism. This work is supported in part by CICYT projects FPA2003-03801 and FPA2006-05807, by EU network "UniverseNet" MRTN-CT-2006-035863 and by CAM project HEPHACOS S-0505/ESP-0346. D.G.F. and A.S. acknowledges support from a FPU-Fellowship from the Spanish M.E.C. We also acknowledge use of the MareNostrum Supercomputer under project AECT-2007-1-0005.

[1] R. A. Hulse and J. H. Taylor, Astrophys. J. **195**, L51 (1975); Nobel Prize in Physics 1993, `http://nobelprize.org/nobel_prizes/physics/laureates/1993/`

[2] M. Maggiore, Phys. Rept. **331**, 283 (2000); C. J. Hogan, arXiv:astro-ph/0608567; A. Buonanno, "Gravitational waves," arXiv:0709.4682 [gr-qc].

[3] A. A. Starobinsky, JETP Lett. **30**, 682 (1979) [Pisma Zh. Eksp. Teor. Fiz. **30**, 719 (1979)].

[4] B. Abbott *et al.* [LIGO Scientific Collaboration], Astrophys. J. **659**, 918 (2007) [arXiv:astro-ph/0608606]. LIGO Home Page: `http://www.ligo.caltech.edu/`

[5] S. A. Hughes, arXiv:0711.0188 [gr-qc]. LISA Home Page: `http://lisa.esa.int`

[6] V. Corbin and N. J. Cornish, Class. Quant. Grav. **23**, 2435 (2006); G. M. Harry, P. Fritschel, D. A. Shaddock, W. Folkner and E. S. Phinney, Class. Quant. Grav. **23**, 4887 (2006). BBO Home Page: `http://universe.nasa.gov/new/program/bbo.html`

[7] S. Kawamura *et al.*, Class. Quant. Grav. **23**, S125 (2006).

[8] M. Kamionkowski, A. Kosowsky and A. Stebbins, Phys. Rev. Lett. **78**, 2058 (1997); U. Seljak and M. Zaldarriaga, Phys. Rev. Lett. **78**, 2054 (1997); Planck Home page: `http://www.rssd.esa.int/Planck`

[9] B. Allen, gr-qc/9604033.

[10] I. H. Stairs, Living Rev. Rel. **6**, 5 (2003).

[11] T. L. Smith, E. Pierpaoli and M. Kamionkowski, Phys. Rev. Lett. **97**, 021301 (2006).

[12] A. Kosowsky, M. S. Turner and R. Watkins, Phys. Rev. Lett. **69**, 2026 (1992), Phys. Rev. D **45**, 4514 (1992); A. Kosowsky and M. S. Turner, Phys. Rev. D **47**, 4372 (1993); M. Kamionkowski, A. Kosowsky and M. S. Turner, Phys. Rev. D **49**, 2837 (1994).

[13] A. Nicolis, Class. Quant. Grav. **21**, L27 (2004); C. Grojean and G. Servant, arXiv:hep-ph/0607107.

[14] A. Kosowsky, A. Mack and T. Kahniashvili, Phys. Rev. D **66**, 024030 (2002); A. D. Dolgov, D. Grasso and A. Nicolis, Phys. Rev. D **66**, 103505 (2002). G. Gogoberidze, T. Kahniashvili and A. Kosowsky, "The spectrum of gravitational radiation from primordial turbulence," arXiv:0705.1733 [astro-ph].

[15] A. Nishizawa *et al.*, "Laser-interferometric Detectors for Gravitational Wave Background at 100 MHz : Detector Design and Sensitivity," arXiv:0710.1944 [gr-qc]; A. M. Cruise and R. M. J. Ingley, Class. Quant. Grav. **23**, 6185 (2006).

[16] L. Kofman, A. D. Linde and A. A. Starobinsky, Phys. Rev. Lett. **73**, 3195 (1994); L. Kofman, A. D. Linde and A. A. Starobinsky, Phys. Rev. D **56**, 3258 (1997).

[17] K. S. Thorne, "*Gravitational Radiation*" in "300 Hundred Years of Gravitation", 330-458.

[18] J. Garcia-Bellido and D. G. Figueroa, Phys. Rev. Lett. **98**, 061302 (2007) [arXiv:astro-ph/0701014].

[19] D. H. Lyth and A. Riotto, Phys. Rept. **314**, 1 (1999).

[20] D. N. Spergel *et al.*, astro-ph/0603449; M. Tegmark *et al.*, astro-ph/0608632; W. H. Kinney, E. W. Kolb, A. Melchiorri and A. Riotto, Phys. Rev. D **74**, 023502 (2006). H. Peiris and R. Easther, astro-ph/0609003.

[21] S. Y. Khlebnikov and I. I. Tkachev, Phys. Rev. D **56**, 653 (1997).

[22] J. Garcia-Bellido, arXiv:hep-ph/9804205.

[23] R. Easther and E. A. Lim, JCAP **0604**, 010 (2006).

[24] R. Easther, J. T. . Giblin and E. A. Lim, "Gravitational Wave Production At The End Of Inflation," arXiv:astro-ph/0612294.

[25] J. F. Dufaux, A. Bergman, G. N. Felder, L. Kofman and J. P. Uzan, arXiv:0707.0875 [astro-ph].

[26] F. Pegoraro, L. A. Radicati, P. Bernard and E. Picasso, Phys. Lett. A **68**, 165 (1978); G. Gemme, A. Chincarini, R. Parodi, P. Bernard and E. Picasso, gr-qc/0112021; R. Ballantini *et al.*, gr-qc/0502054.

[27] A. D. Linde, Phys. Rev. D **49**, 748 (1994); J. Garcia-Bellido and A. D. Linde, Phys. Rev. D **57**, 6075 (1998).

[28] G. N. Felder, J. Garcia-Bellido, P. B. Greene, L. Kofman, A. D. Linde and I. Tkachev, Phys. Rev. Lett. **87**, 011601 (2001); G. N. Felder, L. Kofman and A. D. Linde, Phys. Rev. D **64**, 123517 (2001).

[29] J. Garcia-Bellido, M. Garcia Perez and A. Gonzalez-Arroyo, Phys. Rev. D **67**, 103501 (2003);

[30] J. Garcia-Bellido and E. Ruiz Morales, Phys. Lett. B **536**, 193 (2002).

[31] J. Garcia-Bellido, D. Y. Grigoriev, A. Kusenko and M. E. Shaposhnikov, Phys. Rev. D **60**, 123504 (1999). J. Garcia-Bellido, M. Garcia-Perez and A. Gonzalez-

Arroyo, Phys. Rev. D **69**, 023504 (2004); A. Tranberg and J. Smit, JHEP **0311**, 016 (2003).

[32] A. Diaz-Gil, J. Garcia-Bellido, M. Garcia Perez and A. Gonzalez-Arroyo, PoS **LAT2005**, 242 (2006); PoS **LAT2007**, 052 (2007), arXiv:0710.0580 [hep-lat].

[33] MareNostrum Supercomputer Home Page: `http://www.bsc.es/`

[34] IFT cluster Home Page: `http://lattice.ft.uam.es/iftcluster/`

[35] G. N. Felder and I. Tkachev, arXiv: hep-ph/0011159; `http://www.science.smith.edu/departments/Physics/fstaff/gfelder/latticeeasy/`

[36] J. Garcia-Bellido, A. D. Linde and D. Wands, Phys. Rev. D **54**, 6040 (1996).

[37] R. Allahverdi, K. Enqvist, J. Garcia-Bellido and A. Mazumdar, Phys. Rev. Lett. **97**, 191304 (2006); R. Allahverdi, K. Enqvist, J. Garcia-Bellido, A. Jokinen and A. Mazumdar, JCAP **0706** (2007) 019 [arXiv:hep-ph/0610134].

[38] S. Y. Khlebnikov and I. I. Tkachev, Phys. Rev. Lett. **77**, 219 (1996); **79**, 1607 (1997); T. Prokopec and T. G. Roos, Phys. Rev. D **55**, 3768 (1997).

[39] V. F. Mukhanov, H. A. Feldman and R. H. Brandenberger, Phys. Rept. **215**, 203 (1992).

[40] S. Carroll, "*Spacetime and Geometry: An introduction to General Relativity*," Addison Wesley (2003).

[41] K. G. Wilson, Phys. Rev. D **10**, 2445 (1974).

[42] F. Cooper, S. Habib, Y. Kluger, E. Mottola, J. P. Paz and P. R. Anderson, Phys. Rev. D **50**, 2848 (1994) [arXiv:hep-ph/9405352]; F. Cooper, S. Habib, Y. Kluger and E. Mottola, Phys. Rev. D **55**, 6471 (1997) [arXiv:hep-ph/9610345].

[43] D. Boyanovsky, D. Cormier, H. J. de Vega, R. Holman, A. Singh and M. Srednicki, Phys. Rev. D **56**, 1939 (1997) [arXiv:hep-ph/9703327]; D. Boyanovsky, H. J. de Vega, R. Holman and J. Salgado, Phys. Rev. D **59**, 125009 (1999) [arXiv:hep-ph/9811273].

[44] J. Baacke, K. Heitmann and C. Patzold, Phys. Rev. D **55**, 2320 (1997) [arXiv:hep-th/9608006]; Phys. Rev. D **55**, 7815 (1997) [arXiv:hep-ph/9612264]; Phys. Rev. D **56**, 6556 (1997) [arXiv:hep-ph/9706274].

[45] J. M. Bardeen, J. R. Bond, N. Kaiser and A. S. Szalay, Astrophys. J. **304**, 15 (1986).

[46] R. Micha and I. I. Tkachev, Phys. Rev. Lett. **90**, 121301 (2003); Phys. Rev. D **70**, 043538 (2004).

[47] http://lattice.ft.uam.es/gw

[48] S. Weinberg, "*Gravitation and Cosmology*", John Wiley & Sons, 1972.

[49] P. B. Greene, L. Kofman, A. D. Linde and A. A. Starobinsky, Phys. Rev. D **56**, 6175 (1997) [arXiv:hep-ph/9705347].

[50] A. J. Farmer and E. S. Phinney, Mon. Not. Roy. Astron. Soc. **346**, 1197 (2003).

[51] J. F. Dufaux, G. N. Felder, L. Kofman, M. Peloso and D. Podolsky, JCAP **0607**, 006 (2006).

[52] G. N. Felder and L. Kofman, Phys. Rev. D **63**, 103503 (2001).

[53] T. L. Smith, M. Kamionkowski and A. Cooray, Phys. Rev. D **73**, 023504 (2006).